

# The Kinematics and Dynamics of the Globular Clusters and Planetary Nebulae of NGC 5128

Kristin A. Woodley

*Department of Physics & Astronomy, McMaster University, Hamilton ON L8S 4M1,  
Canada*

woodleka@physics.mcmaster.ca

William E. Harris

*Department of Physics & Astronomy, McMaster University, Hamilton ON L8S 4M1,  
Canada*

harris@physics.mcmaster.ca

Michael A. Beasley

*Instituto de Astrofísica de Canarias, Calle Vía Láctea, s/n E-38200, La Laguna Tenerife,  
Spain*

beasley@iac.es

Eric W. Peng

*Herzberg Institute of Astrophysics, 5071 West Saanich Road, Victoria, BC V8V 2X6,  
Canada*

eric.peng@nrc-cnrc.gc.ca

Terry J. Bridges

*Department of Physics, Queen's University, Kingston, ON K7L 3N6, Canada*

tjb@astro.queensu.ca

Duncan A. Forbes

*Centre for Astrophysics & Supercomputing, Swinburne University, Hawthorn, VIC 3122,  
Australia*

dforbes@astro.swin.edu.au

Gretchen L. H. Harris

*Department of Physics & Astronomy, University of Waterloo, Waterloo ON N2L 3G1,  
Canada*

glharris@astro.uwaterloo.ca

## ABSTRACT

A new kinematic and dynamic study of the halo of the giant elliptical galaxy NGC 5128 is presented. From a spectroscopically confirmed sample of 340 globular clusters and 780 planetary nebulae, the rotation amplitude, rotation axis, velocity dispersion, and total dynamical mass are determined for the halo of NGC 5128. The globular cluster kinematics were searched for both radial dependence and metallicity dependence by subdividing the globular cluster sample into 158 metal-rich ( $[\text{Fe}/\text{H}] > -1.0$ ) and 178 metal-poor ( $[\text{Fe}/\text{H}] < -1.0$ ) globular clusters. Our results show that the kinematics of the metal-rich and metal-poor subpopulations are quite similar: over a projected radius of 0 – 50 kpc, the mean rotation amplitudes are  $47 \pm 15$  and  $31 \pm 14$  km s<sup>-1</sup> for the metal-rich and metal-poor populations, respectively. There is a indication within 0 – 5 kpc that the metal-poor clusters have a lower rotation signal than in the outer regions of the galaxy. The rotation axis shows an interesting twist at 5 kpc, agreeing with the zero-velocity curve presented by Peng and coworkers. Within 5 kpc, both metal-rich and metal-poor populations have a rotation axis nearly parallel to the north-south direction, which is 0°, while beyond 5 kpc the rotation axis twists  $\sim 180^\circ$ . The velocity dispersion displays a steady increase with galactocentric radius for both metallicity populations, with means of  $111 \pm 6$  and  $117 \pm 6$  km s<sup>-1</sup> within a projected radius of 15 kpc for the metal-rich and metal-poor populations; however, the outermost regions suffer from low number statistics and spatial biases. The planetary nebula kinematics are slightly different. Out to a projected radius of 90 kpc from the center of NGC 5128, the planetary nebulae have a higher rotation amplitude of  $76 \pm 6$  km s<sup>-1</sup>, and a rotation axis of  $170 \pm 5^\circ$  east of north, with no significant radial deviation in either determined quantity. The velocity dispersion decreases with galactocentric distance. The total mass of NGC 5128 is found using the tracer mass estimator, described by Evans et al., to determine the mass supported by internal random motions and the spherical component of the Jeans equation to determine the mass supported by rotation. We find a total mass of  $1.0 \pm 0.2 \times 10^{12} M_\odot$  from the planetary nebula data extending to a projected radius of 90 kpc. The similar kinematics of the metal-rich and metal-poor globular clusters allow us to combine the two subpopulations

to determine an independent estimate of the total mass, giving  $1.3 \pm 0.5 \times 10^{12} M_{\odot}$  out to a projected radius of 50 kpc. Lastly, we publish a new and homogeneous catalog of known globular clusters in NGC 5128. This catalog combines all previous definitive cluster identifications from radial velocity studies and *HST* imaging studies, as well as 80 new globular clusters with radial velocities from a study of M.A. Beasley et al. (in preparation).

*Subject headings:* galaxies: elliptical and lenticular, cD — galaxies: individual (NGC 5128) — galaxies: kinematics and dynamics — galaxies: star clusters — globular clusters: general — planetary nebulae: general — catalogs

## 1. Introduction

Globular clusters (GCs), as single-age, single-metallicity objects, are excellent tracers of the formation history of their host galaxies, through their dynamics, kinematics, metallicities, and ages. For most galaxies within  $\simeq 20$  Mpc, GCs can be identified through photometry and image morphology, from which follow-up radial velocity studies can be carried out with multi-object spectroscopy on 4 and 8 m class telescopes. The ability to target hundreds of objects in a single field has vastly increased the observed samples of GCs confirmed in many galaxies, providing the necessary basis for detailed kinematic and age studies.

Another benefit of using GCs as a kinematic tracer is that they provide a useful, independent basis for comparison with results from planetary nebulae (PNe). This is particularly true given the current debate surrounding the use of PN velocities and the implications for low dark matter halos. For example, Romanowsky et al. (2003) reported, based on PN velocities, that three low-luminosity ellipticals revealed declining velocity dispersion profiles and little or no dark matter. However, subsequent simulations of merger-remnant ellipticals suggested that the radial anisotropy of intermediate-age PNe could give rise to the observed profiles within standard halos of dark matter (Dekel et al. 2005; Mamon & Lokas 2005). Flattening of the galaxy along the line of sight is another possible explanation. One of the ellipticals studied by Romanowsky et al. (2003), NGC 3379, has also been investigated using GC kinematics (Pierce et al. 2006; Bergond et al. 2006); both studies found evidence of a dark matter halo. But the two studies of NGC 3379 suffered from small number statistics. Clearly there is a need to directly compare PN and GC kinematics for the same elliptical with sufficiently large numbers of tracer objects.

Previous velocity-based studies of globular cluster systems (GCSs) have shown an intriguing variety of results in their overall kinematics. Prominent recent examples include the

following:

1. Côté et al. (2001) performed a kinematic analysis of the GCS in M87 (NGC 4486), the cD galaxy in the Virgo Cluster. With a sample of 280 GCs, they showed that the entire GCS rotates on an axis matching the photometric *minor* axis of the galaxy, except for the inner metal-poor sample. Inside the onset of the cD envelope, the metal-poor clusters appear to rotate around the *major* axis of the galaxy instead. This study also found evidence for an increase in velocity dispersion,  $\sigma_v$ , with radius, due to the larger scale Virgo Cluster mass distribution. They also showed no strong evidence for a difference in  $\sigma_v$  between the metal-poor and metal-rich groups. Using a Virgo mass model, they investigated anisotropy and found that as a whole, the GCS had isotropy, but considered separately, the metal-poor and metal-rich subpopulations had slight anisotropy.

2. Côté et al. (2003) performed a dynamical analysis for M49 (NGC 4472), the other supergiant member of the Virgo Cluster. Using over 260 GCs, they found that the metal-rich population shows no strong evidence for rotation, while the metal-poor population does rotate about the minor axis of the galaxy. In addition, they found that the metal-poor clusters had an overall higher dispersion than the metal-rich population.

3. Richtler et al. (2004) determined the kinematics for the GCS in NGC 1399, the brightest elliptical in the Fornax Cluster of galaxies. Armed with a sample of over 460 GCs, they found a marginal rotation signal for the entire GC sample and the outer metal-poor sample, while no rotation was seen for the metal-rich subpopulation. Their projected velocity dispersion showed no radial trend within their determined uncertainty, but the metal-poor clusters had a higher dispersion than the metal-rich clusters. The kinematics of the PNe in NGC 1399 have been most recently studied by Saglia et al. (2000) and Napolitano et al. (2002) using a small sample of 37 PNe from Arnoaboldi et al. (1994). These studies do not indicate any significant deviations in velocity dispersion with radius for the PNe, yet interestingly, Napolitano et al. (2002) found strong rotation for the PNe in the inner region of the galaxy.

4. Peng, Ford & Freeman (2004c) studied the GC kinematics of the giant elliptical NGC 5128 from a total of 215 GCs. Their results showed definite rotation signals in both metallicity groups beyond a 5 kpc distance from the center of the galaxy, as well as similar velocity dispersions in both the metal-poor and the metal-rich populations within a 20 kpc projected radius. A similar PN kinematic study in NGC 5128 (Peng, Ford & Freeman 2004b) showed that the PNe population is rotating around a twisted axis that turns just beyond the 5 kpc distance.

These few detailed kinematic studies of GCSs in elliptical galaxies, show results that

appear to differ on a galaxy-by-galaxy basis, without any clear global trends. The age distributions of the GC populations in these same galaxies tend to show a consistent pattern in which the blue, or metal-poor, population is found to be universally old. The red, or metal-rich, population has also been shown to be old in the study of Strader et al. (2005). Their study found that *both* the metal-poor and metal-rich GCs in a sample of eight galaxies ranging from dwarf to massive ellipticals, all have ages as old as their Galactic GC counterparts. Conversely, in a small sample of studies, the red GC population has also been found to be 2-4 Gyr younger than the metal-poor GC population, and with a wider spread in determined ages (see the studies of Peng, Ford & Freeman 2004c; Puzia et al. 2005, among others), although this is not yet a well-established trend. The GCs in NGC 5128 appear to be old, with an intermediate-age population (Peng, Ford & Freeman 2004c; Beasley et al. 2006).

NGC 5128 (Centaurus A), the central giant in the Centaurus group of galaxies at a distance of only  $\sim 4$  Mpc, is a prime candidate for both kinematic and age studies. Its GCS has a specific frequency of  $S_N \simeq 2.2 \pm 0.6$  (Harris et al. 2006), toward the low end of the giant elliptical range but about twice as high as in typical disk galaxies. Its optical features show faint isophotal shells located in the halo (e.g. Peng et al. 2002), the prominent dust lane in the inner 5 kpc, the presence of gas, and star formation, all of which suggest that NGC 5128 could be a merger product. Baade & Minkowski (1954) first suggested that NGC 5128 could be the result of a merger between two galaxies, a spiral and an elliptical. This idea was followed by the general formation mechanism of disk-disk mergers proposed by Toomre & Toomre (1972). Bekki, Harris, & Harris (2003) found that the metallicity distribution function of the halo field stars could be reproduced by a gas-free (“dry”) disk-disk merger scenario. Recent numerical simulations by Bekki & Peng (2006) also demonstrate that the PN kinematics observed in NGC 5128 (Peng, Ford & Freeman 2004b) can be reproduced relatively well from a merger of unequal-mass disk galaxies (with one galaxy half the mass of the other) colliding on a highly inclined orbital configuration.

Alternatively, much of NGC 5128 could be a “red and dead” galaxy, passively evolving since its initial formation as a large seed galaxy (Woodley 2006), while undergoing later minor mergers and satellite accretions. Evidence consistent with this scenario is in the halo population of stars in NGC 5128, which have a mean age of  $8_{-3.5}^{+3.0}$  Gyr (Rejkuba et al. 2005). Its metal-poor GC ages have also been shown to have ages similar to Milky Way GCs, while the metal-rich population appears younger (Peng, Ford & Freeman 2004c). Our new spectroscopic study (Beasley et al. 2006) suggests that NGC 5128 has a trimodal distribution of cluster ages:  $\sim 50\%$  of metal-rich clusters have ages of 6 – 8 Gyr, only a small handful of metal-rich clusters have ages of 1 – 3 Gyr, and a large fraction of both metal-rich and metal-poor clusters have ages of  $\simeq 12$  Gyr. Lastly, the halo kinematics of NGC 5128 have also been recently shown to match the surrounding satellite galaxies in the low-density

Centaurus group, suggesting that NGC 5128 acts like an inner component to its galaxy group (Woodley 2006). Kinematic and age studies with large number of GCs are thus starting to help disentangle the formation of this giant elliptical.

The confirmed GC population in NGC 5128 is now large enough to allow a new kinematic analysis subdivided to explore radial and metallicity dependence, while avoiding small number statistics in almost all regions of the galaxy. The analysis presented here complements the detailed age distribution study provided by Beasley et al. (2006). The results provide a broader picture of the formation scenario of NGC 5128.

The sections of this paper are divided as follows: § 2 contains the full catalog of NGC 5128 GCs with known photometry and radial velocities, § 3 contains the kinematic analysis of GCs, § 4 contains the kinematic analysis of the PN population, § 5 contains the discussion of the dynamical mass of NGC 5128, and § 6 contains our final discussion, as well as concluding remarks.

## 2. The Catalog of Globular Clusters in NGC 5128

Finding GCs in NGC 5128 is challenging. This process begins with photometric surveys of the many thousands of objects projected onto the NGC 5128 field (e.g. Rejkuba 2001; Harris et al. 2004); only a few percent of these are the GCs that we seek. This daunting task is made difficult by the galactic latitude of NGC 5128 ( $b = 19^\circ$ ), which means that many foreground stars are present in the field of NGC 5128. Background galaxies are another major contaminant in the field, forcing the use of search criteria such as magnitude, color, and object morphology to help build the necessary candidate list of GCs. Confirmation of such candidate objects can then be done with spectroscopic radial velocity measurements. The GCs in NGC 5128 have radial velocities in the range  $v_r = 200 - 1000 \text{ km s}^{-1}$ , while most foreground stars have  $v_r < 200 \text{ km s}^{-1}$ . Background galaxies have radial velocities of many thousands of  $\text{km s}^{-1}$  and can easily be eliminated (see the recent studies of Peng, Ford, & Freeman 2004a; Woodley, Harris, & Harris 2005).

Over the past quarter century, there have been seven distinct radial velocity studies to identify GCs in NGC 5128 (van den Bergh, Hesser, & Harris 1981; Hesser et al. 1984; Hesser, Harris, & Harris 1986; Harris et al. 1992; Peng, Ford, & Freeman 2004a; Woodley, Harris, & Harris 2005; Beasley et al. 2006). Although Harris et al. (1992) was not a radial velocity study itself, but rather a CCD photometric study of previously confirmed GCs, it does include the GCs determined spectroscopically from Sharples (1988). A recent study with measured GC radial velocities published by Rejkuba et al. (2007) has confirmed two new GCs, HCH15 and

R122, included in our catalog.

Within this catalog are 80 new GCs with radial velocity measurements from Beasley et al. (2006). The combination of these studies now leads to a confirmed population of 342 GCs.<sup>1</sup> Also included in our catalog are the new GC candidates from *HST* STIS imaging from Harris et al. (2002), labelled C100-C106, and from *HST* ACS imaging from Harris et al. (2006), labelled C111-C179. All these previous studies have their own internal numbering systems, which makes the cluster identifications somewhat confusing at this point. Here we define a new, homogeneous listing combining all this material and with a single numbering system.

Our catalog of the GCs of NGC 5128 is given in Table 1. In successive columns, the Table gives the new cluster name in order of increasing right ascension; the previous names of the cluster in the literature; right ascension and declination (J2000); the projected radius from the center of NGC 5128 in arcminutes; the  $U$ ,  $B$ ,  $V$ ,  $R$ , and  $I$  photometric indices and their measured uncertainties; the  $C$ ,  $M$ , and  $T_1$  photometric indices and their uncertainties; the colors  $U-B$ ,  $B-V$ ,  $V-R$ ,  $V-I$ ,  $M-T_1$ ,  $C-M$ , and  $C-T_1$ ; and, lastly, the weighted mean velocity  $v_r$  and its associated uncertainty from all previous studies. All  $UBVRI$  photometry is from the imaging survey described in Peng, Ford, & Freeman (2004a). The  $CMT_1$  data are from Harris et al. (2004).

The mean velocities are weighted averages with weights on each individual measurement equal to  $\varepsilon_v^{-2}$  where  $\varepsilon_v$  is the quoted velocity uncertainty from each study. The uncertainty in the mean velocity is then  $\langle \varepsilon_v \rangle = (\sum \varepsilon_i^{-2})^{-1/2}$ . There are no individual uncertainties supplied for the velocities for clusters studied by Hesser, Harris, & Harris (1986), but their study reports that the mean velocity uncertainty for clusters with  $R_{gc} < 11'$  is  $25 \text{ km s}^{-1}$  and for  $R_{gc} > 11'$  is  $44 \text{ km s}^{-1}$ . We have adopted these values accordingly for their clusters.<sup>2</sup>

The study by Harris et al. (1992) also does not report velocity uncertainties; however, these clusters have all been recently measured by Peng, Ford, & Freeman (2004a). The rms

---

<sup>1</sup>The confirmed GC list in Woodley (2006) containing 343 GCs has been reduced to 340 based on recent spectroscopic and imaging studies. Object 304867 with a high radial velocity of  $305 \pm 56 \text{ km s}^{-1}$  appears to be an M-type star based on the strong molecular bands in its spectrum, see Beasley et al. (2006) for further discussion. Objects pff\_gc-010 and 114993 are also rejected as GCs because of their starlike appearance under *HST* ACS imaging; see Harris et al. (2006). However, newly confirmed GCs HCH15 and R122 have now been added (Rejkuba et al. 2007).

<sup>2</sup>Hesser, Harris, & Harris (1986) report C32 at a distance of  $R_{gc} = 10.8'$ , but more recently Peng, Ford, & Freeman (2004a) claim a distance of  $R_{gc} = 11.25'$ , so it has an adopted uncertainty of  $44 \text{ km s}^{-1}$  in the weighted mean.

scatter of the Harris et al. (1992) values from theirs was  $58 \text{ km s}^{-1}$ . This value has been adopted as the velocity uncertainty of the Harris et al. (1992) clusters in the weighted means.

The weighted mean velocity of cluster C10 does not include the measured value determined by Peng, Ford, & Freeman (2004a) which is significantly different from other measurements. Also, cluster C27 does not include the measurement of  $v_r = 1932 \pm 203 \text{ km s}^{-1}$  from Beasley et al. (2006), indicating that this object is a galaxy. We include C27 as a GC, but with caution.

In the weighted velocity calculations, the velocities and uncertainties of the 27 GCs from Rejkuba et al. (2007) have been rounded to the nearest whole number, with any velocity uncertainty below  $1 \text{ km s}^{-1}$  rounded up to a value of 1.

Lastly, the GC pff\_gc-089 overlaps the previously existing confirmed cluster, C49, within a  $0.5''$  radius; pff\_gc-089 is therefore removed from the catalog of confirmed GCs.

The data in Table 1 provide the basis for the kinematic study presented in this paper. We use them to derive the rotation amplitude, rotation axis and velocity dispersion in the full catalog of clusters, as well as for the metal-poor ( $[\text{Fe}/\text{H}] < -1$ ) and metal-rich ( $[\text{Fe}/\text{H}] > -1$ ) subpopulations. For this purpose, we define the metallicity of the GCs by transforming the dereddened colors  $(C - T_1)_o$  to  $[\text{Fe}/\text{H}]$  through the standard conversion (Harris & Harris 2002), calibrated through Milky Way cluster data. A foreground reddening value of  $E(B - V) = 0.11$  for NGC 5128, corresponding to  $E(C - T_1) = 0.22$ , has been adopted. The division of  $[\text{Fe}/\text{H}] = -1$  between metal-rich and metal-poor GCs has been shown as a good split between the two metallicity populations from  $[\text{Fe}/\text{H}]$  values converted from  $C - T_1$  in Woodley, Harris, & Harris (2005) and Harris et al. (2004) for NGC 5128. If no  $C$  and/or  $T_1$  values are available for the cluster, it is classified as metal-rich or metal-poor through a transformation from  $(U - B)_o$  to  $[\text{Fe}/\text{H}]$  from Reed, Harris, & Harris (1994).

In Figure 1 we show the spatial distributions of all the GCs from Table 1 (*left*) and the distribution of the known PNe (*right*). Both systems are spatially biased to the major axis of the galaxy because this is where most of the GC and PN searches have concentrated.

### 3. Kinematics of the Globular Cluster System

#### 3.1. Velocity Field

For the present discussion we adopt a distance of 3.9 Mpc for NGC 5128. This value is based on four stellar standard candles that each have internal precisions near  $\pm 0.2 \text{ mag}$ : the PN luminosity function, the tip of the old-halo red giant branch, the long-period variables,



and the Cepheids (Harris et al. 1999; Rejkuba 2004; Ferrarese et al. 2006).

HCH15 and R122 have not been included in our kinematic study, as our study was completed before publication of these velocities. The weighted velocities used in this kinematic study do not include the most recent 25 velocities of previously known GCs published in Rejkuba et al. (2007). Note that the velocities published in Table 1 do, however, include the Rejkuba et al. (2007) velocities in the quoted final weighted radial velocities for completeness.

The velocity distribution of the entire sample of 340 is shown in Figure 2 (*top left*), binned in  $50 \text{ km s}^{-1}$  intervals. A fit with a single Gaussian yields a mean velocity of  $546 \pm 7 \text{ km s}^{-1}$ , nicely matching the known systemic velocity of  $541 \pm 7 \text{ km s}^{-1}$  (Hui et al. 1995). There is a slight asymmetry at the low-velocity end that is likely due to contamination by a few metal-poor Milky Way halo stars (also seen in the metal-poor subpopulation in the bottom left panel, which has a mean velocity determined by the Gaussian fit as  $532 \pm 13 \text{ km s}^{-1}$ ).

Selecting the clusters with radial velocity uncertainties less than  $50 \text{ km s}^{-1}$  leaves 226 clusters, plotted in Fig. 2 (*top right*). The close fit to a single Gaussian is consistent with an isotropic distribution of orbits; the mean velocity is  $554 \pm 5 \text{ km s}^{-1}$ . The metal-rich population, with a mean velocity determined by the Gaussian fit of  $565 \pm 11 \text{ km s}^{-1}$ , is plotted in the bottom right panel, and also shows no strong asymmetries.

Looking closer at the metal-poor velocity asymmetry, we note that the 15 metal-poor clusters between 250 and  $300 \text{ km s}^{-1}$  (in the region where contamination by Milky Way field stars could occur) are balanced by only two GCs at the high-velocity end on reflection across the systemic velocity. The same velocity regions in the metal-rich population are nearly equally balanced with four clusters between 250 and  $300 \text{ km s}^{-1}$  with three clusters at the reflected high-velocity range. Interestingly, the four metal-rich clusters between 250 and  $300 \text{ km s}^{-1}$  have projected radii  $> 17 \text{ kpc}$  even though the metal-rich population is more centrally concentrated than the metal-poor (see Peng, Ford & Freeman 2004c; Woodley, Harris, & Harris 2005, among others). The metal-poor clusters between 250 and  $300 \text{ km s}^{-1}$ , conversely, are more evenly distributed, with five clusters between projected radii of 5 and 10 kpc, five clusters between 10 and 20 kpc, and five clusters beyond 20 kpc from the center of NGC 5128. Some of these low-velocity, metal-poor objects could be foreground stars with velocities in the realm of GCs in NGC 5128 ( $v_r \gtrsim 250 \text{ km s}^{-1}$ ). However, with only 340 GCs currently confirmed within  $\sim 45'$  from the center of NGC 5128, out of an estimated  $\simeq 1500$  total clusters within  $25'$  (Harris et al. 2006), these metal-poor, low-velocity objects could simply be part of a very incomplete GC sample that is also spatially biased. This potential bias is clearly shown in Figure 3, which shows the projected radial

distribution as a function of azimuthal angle for our GC sample. Beyond 12 kpc, the two "voids" coincide with the photometric minor axis of the galaxy, attributed at least partly to incomplete cluster surveys in these regions. These objects should, therefore, not be dropped from the GC catalog without further spectroscopic analysis.

### 3.2. Rotation Amplitude, Rotation Axis, and Velocity Dispersion

#### 3.2.1. Mathematic and Analytic Description

We determine the rotation amplitude and axis of the GCS of NGC 5128 from

$$v_r(\Theta) = v_{sys} + \Omega R \sin(\Theta - \Theta_o) \quad (1)$$

(see Côté et al. 2001; Richtler et al. 2004; Woodley 2006). In Equation 1,  $v_r$  is the observed radial velocity of the GCs in the system,  $v_{sys}$  is the galaxy's systemic velocity,  $R$  is the projected radial distance of each GC from the center of the system assuming a distance of 3.9 Mpc to NGC 5128, and  $\Theta$  is the projected azimuthal angle of the GC measured in degrees east of north. The systemic velocity of NGC 5128 is held constant at  $v_{sys} = 541$  km s<sup>-1</sup> (Hui et al. 1995) for all kinematic calculations. The rotation axis of the GCs,  $\Theta_o$ , and the product  $\Omega R$ , the rotation amplitude of the GCs in the system, are the values obtained from the numerical solution. We use a Marquardt-Levenberg non-linear fitting routine (Press et al. 1992).

Eqn. 1 assumes spherical symmetry. While this may be a decent assumption for the inner 12 kpc region (it has a low ellipticity of  $\sim 0.2$ ; Peng, Ford & Freeman 2004b), true ellipticities for the outer regions of the system are not well known because of the sample bias (see Fig. 3). Future studies to remove these biases are vital to obtaining a sound kinematic solution for the entire system. Eqn. 1 also assumes that  $\Omega$  is only a function of the projected radius and that the rotation axis lies in the plane of the sky. It is not entirely clear how these assumptions, discussed thoroughly in Côté et al. (2001), apply to the GC and PN systems of NGC 5128. The  $\Omega$  we solve for is, therefore, only a lower limit to the true  $\Omega$  if the true rotation axis is not in the plane of the sky.

The projected velocity dispersion is also calculated from the normal condition,

$$\sigma_v^2 = \sum_{i=1}^N \frac{(v_{f_i} - v_{sys})^2}{N} \quad (2)$$

where  $N$  is the number of clusters in the sample,  $v_{f_i}$  is the GC's radial velocity *after subtraction of the rotational component determined with Eqn. 1*, and  $\sigma_v$  is the projected velocity dispersion.

The GCs were assigned individual weights in the sums that combine in quadrature the individual observational uncertainty,  $\varepsilon_v$ , in  $v_r$  and the random velocity component,  $\varepsilon_{random}$ , of the GCS. The dominance of the latter is evident by the large dispersion in the GC velocities in the kinematic fitting (see Figure 4). In other words, the clusters have individual weights,  $\omega_i = (\varepsilon_v^2 + \varepsilon_{random}^2)^{-1}$ ; the main purpose of this is to assign a bit more importance to the clusters with more securely measured velocities. This random velocity term dominates in nearly every case, leaving the GCs with very similar base weights in the kinematic fitting.

The three kinematic parameters - rotation amplitude, rotation axis, and velocity dispersion - are determined with three different binning methods. The first involves binning the GCs in radially projected circular annuli from the center of NGC 5128. The chosen bins keep a minimum of 15 clusters in each, ranging as high as 124 clusters. The bins are 0-5, 5-10, 10-15, 15-25, and 25-50 kpc. Also, we include 0-50 kpc to determine the overall kinematics of the system.

The second method adopts bins with equal numbers of clusters. The entire population of clusters had nine bins of 38 clusters each, the metal-poor clusters had nine bins of 20 clusters, and the metal-rich clusters had eight bins of 20 clusters. The base weighting is applied to the clusters in both the first and second binning methods.

The third method uses an exponential weighting function, outlined in Bergond et al. (2006), to generate a smoothed profile. This method determines each kinematic parameter at the radial position,  $R$ , of every GC in the entire sample by exponentially weighting all other GCs surrounding that position based on their radial separation,  $R - R_i$ , following

$$w_i(R) = \frac{1}{\sigma_R} \exp\left[-\frac{(R - R_i)^2}{2\sigma_R^2}\right]. \quad (3)$$

In Equation 3,  $w_i$  is the determined weight on each GC in the sample, and  $\sigma_R$  is the half-width of the window size. For this study,  $\sigma_R$  is incrementally varied in a linear fashion for the total sample from  $\sigma_R = 1.0$  kpc at the radius of the innermost GC in the sample out to  $\sigma_R = 4.5$  kpc at the radius of the outermost GC, where the population is lowest. The metal-poor population was given a half-width window of  $\sigma_R = 1.0 - 6.5$  kpc, and the metal-rich population was given a half-width window of  $\sigma_R = 2 - 5.3$  kpc, again from the innermost to outermost cluster. The progressive radial increase in  $\sigma_R$  ensured that each point  $R$  had roughly equal total weights.

### 3.2.2. *Rotation Amplitude of the Globular Cluster System*

The kinematic parameters were determined for the entire sample of 340 GCs, as well as the subpopulations of 178 metal-poor and 158 metal-rich GCs (four clusters have unknown metallicity). The kinematic results for the entire population of GCs are shown in Table 2, reproduced almost in full from Woodley (2006), while the results for the metal-poor and metal-rich clusters are shown in Tables 3 & 4, respectively. The columns give the radial bin, the mean projected radius in the bin, the radius of the outermost cluster, the number of clusters in the bin, the rotation amplitude, the rotation axis, and the velocity dispersion, with associated uncertainties. These are followed by the mass correction, the pressure-supported mass, the rotationally supported mass, and the total mass in units of solar mass (see § 5 for the mass discussion). The results for the alternate two methods, using an equal number of GCs per bin and the exponentially weighted GCs, are not shown in tabular form but are included in all of the figures.

Figure 4 shows the sine fit of Eqn. 1 for the total population and for the metal-poor and metal-rich subpopulations. All three populations show rotation about a similar axis. As discussed in § 3.1, the metal-poor population has more members with low velocities ( $V_r \leq 300 \text{ km s}^{-1}$ ) than the metal-rich population, suggesting possible contamination of Milky Way foreground stars in the sample.

Figures 5 & 6 show the rotation amplitude results for the entire population and for the metal-poor and metal-rich subpopulations, respectively. The three kinematic methods, described in Section 3.2.1, appear to agree relatively well for all three populations of clusters. While there appears to be no extreme difference in rotation amplitude between the cluster populations, the metal-poor subpopulation of clusters has lower rotation in the inner 5 kpc of NGC 5128 than the metal-rich subpopulation. The weighted average of the 0-5 kpc radial bin and the innermost equal-numbered bin, shows that the entire population has a rotation amplitude of  $\Omega R = 31 \pm 17 \text{ km s}^{-1}$ , while the metal-poor population has  $\Omega R = 17 \pm 26 \text{ km s}^{-1}$  and the metal-rich population has  $\Omega R = 57 \pm 22 \text{ km s}^{-1}$ . Peng, Ford & Freeman (2004c) show in their study that the metal-poor population has very little rotation in the central regions, completely consistent with our findings. The rotation amplitude does not appear to differ between the two populations outside of 5 kpc.

### 3.2.3. *Rotation Axis of the Globular Cluster System*

The results of the rotation axis solutions are shown in Figures 7 & 8, again for the entire population and for the metal-poor and metal-rich subpopulations. The solution for

$\Theta_0$  agrees well for all three kinematic methods and all subgroups. The inner 5 kpc region has a different rotation axis than the outer regions, demonstrated clearly in all three binning methods. The innermost bin yields weighted averages of  $\Theta_o = 369 \pm 24^\circ$ ,  $\Theta_o = 25 \pm 55^\circ$ , and  $\Theta_o = 352 \pm 18^\circ$ , all of which are equal within their uncertainties. Beyond 5 kpc, the rotation axes for all three populations are in even closer agreement, with averages of  $\Theta_o = 189 \pm 6^\circ$ ,  $\Theta_o = 199 \pm 7^\circ$ , and  $\Theta_o = 196 \pm 7^\circ$  for the entire population, the metal-poor subpopulation, and the metal-rich subpopulation, respectively. The position angle of the photometric major axis of NGC 5128 is  $\Theta = 35^\circ$  and  $215^\circ$  east of north and the photometric minor axis is  $\Theta = 119^\circ$  and  $299^\circ$  east of north (Dufour et al. 1979). It appears the GCS is rotating about an axis similar to the photometric major axis for the full extent of the galaxy, with a possible axial twist or counterrotation within 5 kpc.

### 3.2.4. *Velocity Dispersion of the Globular Cluster System*

Figures 9 & 10 show the velocity dispersion for the entire population and for the metal-poor and metal-rich subpopulations. Our results for  $\sigma_v$  show no significant differences between the metallicity subpopulations. All three show a relatively flat velocity dispersion ( $\sigma_v = 119 \pm 4$ ,  $\sigma_v = 117 \pm 6$ , and  $\sigma_v = 111 \pm 6$  km s<sup>-1</sup> within 15 kpc of the center of NGC 5128 for the entire population and for the metal-poor and metal-rich subpopulations, respectively). These results match the previous study of NGC 5128 by Peng, Ford & Freeman (2004c), whose determined velocity dispersion for the GCs within 20 kpc ranged between 75 and 150 km s<sup>-1</sup>. At a larger radius, we find that  $\sigma_v$  then slowly increases to  $\sigma_v > 150$  km s<sup>-1</sup> towards the outer regions of the halo for all populations. The velocity dispersion of the metal-rich GCs, interestingly, appears higher than that of the metal-poor GCs in the outer regions (although still consistent within the determined uncertainties). In most previous studies, the velocity dispersion of the metal-poor GCs usually appears higher than that of the metal-rich GCs, if there is a notable velocity dispersion difference between the subpopulations (see the studies of Côté et al. 2003; Richtler et al. 2004, as examples).

To explore the cause of the distinct rise past 15 kpc a bit further, we have plotted the actual velocity histograms in Figure 11 for the metal-poor and metal-rich subgroups, subdivided further into inner ( $R < 15$  kpc) and outer ( $R > 15$  kpc) regions. In the inner 15 kpc, both samples show histograms strongly peaked near  $v_f = 0$  and with at least roughly Gaussian falloff to both high and low velocities. By contrast, the histograms for the outer regions (15 – 50 kpc) are noticeably flatter, so that the clusters with larger velocity residuals have relatively more importance to the formal value of  $\sigma_v$ . Nominally, the flatter shape of the velocity distribution would mean that the outer-halo clusters display anisotropy in

the direction of a bias towards more circular orbits. However, such a conclusion would be premature at this point for two reasons. First, the sample size in the outer regions is still too small to lead to high significance, and a direct comparison between the inner and outer histograms (through a Kolmogorov-Smirnov test) does not show a statistically significant difference between them larger than the 70% level. Second, the outer samples may still be spatially biased in favor of objects along the major axis of the halo, as discussed above, and this bias sets in strongly for  $R > 12$  kpc (see Fig. 3), very near where we have set the radial divisions in this Figure. This type of velocity distribution can also arise from the accretions of satellite galaxies with their own small numbers of GCs (Bekki et al. 2003). We will need to have a larger sample of the outer-halo clusters, and one in which these potential sample biases have been removed, before we can draw any firmer conclusions. However, it needs to be explicitly stated that the outermost point in the kinematic plots for the GCs representing 25 – 50 kpc suffers from very high spatial biases and low number statistics ( $< 40$  GCs) and covers a large radial interval. The rise in velocity dispersion could be driven purely by systematic effects resulting from the radial gradient of the number density of GCs in this outermost bin (Napolitano et al. 2001).

#### 4. Kinematics of the Planetary Nebula System of NGC 5128

NGC 5128 has a large number, 780, of identified PNe with measured radial velocity from the studies of Peng, Ford & Freeman (2004b) and Hui et al. (1995); these PNe are projected out to 90 kpc assuming a distance to NGC 5128 of 3.9 Mpc. Since these are also old objects, it is of obvious interest to compare them with the GCS. The PNe also have the advantage of giving us the best available look at the kinematics of the halo field stars.

The PN kinematic results are listed in Table 5, with the same columns as Table 2. The results are shown in Figures 5, 7, & 9 for the rotation amplitude, rotation axis, and velocity dispersion, respectively. The spatial distribution of the known PNe is, like the GCS, biased toward the major axis at large radii (see Fig. 1). Nevertheless, their kinematics closely resemble the GCs.

The kinematics of the PN system are very consistent among all three binning methods. The rotation amplitude and rotation axis show little radial trend, while the velocity dispersion appears relatively flat within the first 15 kpc at  $\sigma_v = 122 \pm 7$  km s<sup>-1</sup> and then slowly *decreases* to  $\sigma_v \simeq 85$  km s<sup>-1</sup> at large galactocentric radius. Peng, Ford, & Freeman (2004a) show that the velocity dispersion of the PNe drops from a central value of 140 to 75 km s<sup>-1</sup> in the outer regions of the galaxy, consistent with the findings of this study. Their velocity field analysis led to the discovery of a "zero-velocity curve" located between the photometric

minor axis,  $119 \pm 5^\circ$  east of north (Dufour et al. 1979), and the north-south direction, for the innermost region of the galaxy. Just beyond 5 kpc, the zero-velocity curve turns and follows a straight line at a  $7^\circ$  angle from the photometric major axis,  $35^\circ$  east of north (Dufour et al. 1979) (see Figure 7 of Peng, Ford & Freeman 2004c).

This study does not show a strong change in rotation axis for the PNe in the innermost regions of the galaxy. However, it clearly shows in all three GC populations a significant change in the rotation axis just beyond 5 kpc from the center of the galaxy. A change in axis of 5 kpc outward ( $\sim 180^\circ$  for the entire population and metal-poor subpopulation and  $\sim 160^\circ$  for the metal-rich subpopulation) has been found, as discussed in § 3.2.3. Similarly, Peng, Ford & Freeman (2004c) show from their sample of 215 clusters that a clear sign of rotation beyond 5 kpc about a misaligned axis appears particularly in their metal-rich subpopulation. The kinematics of the GCs in this study matches the line of zero velocity relatively nicely. Within 5 kpc the rotation axis of the GCS is nearly-parallel to the north-south direction, and beyond 5 kpc the rotation axis is near  $200^\circ$  east of north, which is only  $\sim 10^\circ$  from the zero-velocity curve.

However, the velocity field of NGC 5128 is complex and not entirely captured by these approximate solutions. The two-dimensional velocity field shown in Peng, Ford & Freeman (2004b) (see their Figure 7), shows that the photometric major axis (which happens to be very close to our maximum rotation as discussed above) is only  $7^\circ$  from the line of zero velocity. This could lead to a very asymmetric velocity profile that may not be well fit by the sine curve described in Equation 1. Biased kinematics, especially the rotation axis, may develop from the sine fit that could lead to a higher estimated velocity dispersion.

Hui et al. (1995) similarly studied the kinematics of the PN system in NGC 5128 with a sample of 433 PNe. They obtain a rotation axis of  $344 \pm 10^\circ$ . Our result of  $170 \pm 5^\circ$  east of north is consistent with their findings on comparing their sine curve fit of their PN data in their Figure 11 to our corresponding fit shown in Fig. 4 for the GCS, which shares a similar axis to our PN sample (note that in their study,  $\phi = 0^\circ$  corresponds to our  $\Theta = 305^\circ$  east of north). Our fits both correspond to a positive rotation amplitude for a rotation axis near  $170^\circ$  east of north and a negative rotation axis near  $350^\circ$  east of north. Therefore, the rotation axis quoted in Hui et al. (1995) of  $344 \pm 10^\circ$  corresponds to a *negative* rotation amplitude of approximately  $70 - 75 \text{ km s}^{-1}$  (taken from their Figure 11), nicely matching our result of a positive  $76 \pm 6 \text{ km s}^{-1}$  about an axis of  $170 \pm 5^\circ$  east of north.

## 5. Dynamics of NGC 5128

Both GCs (Côté et al. 2001; Larsen et al. 2002; Evans et al. 2003; Côté et al. 2003; Beasley et al. 2004; Peng, Ford & Freeman 2004c, among others) and PNe (Ciardullo et al. 1993; Hui et al. 1995; Arnaboldi et al. 1998; Peng, Ford & Freeman 2004b, among others) can be used to estimate the total dynamical mass of their host galaxies. A variety of tools are in use including derived mass models, the virial mass estimator (Bahcall & Tremaine 1981), the projected mass estimator (Heisler, Tremaine, & Bahcall 1985), and the tracer mass estimator (Evans et al. 2003).

NGC 5128 does not have a large X-ray halo (detected by Kraft et al. 2003; O’Sullivan, Forbes, & Ponman 2001, the latter reporting a measurement of  $\log L_x = 40.10 \text{ erg s}^{-1}$ ), such as is evident in other giant ellipticals such as M87 (Côté et al. 2001) or NGC 4649 (Bridges et al. 2006). Thus it is difficult to model the dark matter profile of NGC 5128 with *a priori* constraints. Without such a mass model, we turn to the tracer mass estimator for the dynamical mass determination. The tracer mass estimator has the distinct advantage over the virial and projected mass estimators that the tracer population does not have to follow the dark matter density in the galaxy - an extremely useful feature for stellar subsystems such as GCs and PNe that might, in principle, have significantly different radial distributions (see Evans et al. (2003) for extensive discussion). Below, we determine the mass of NGC 5128 using the tracer populations of GCs and PNe (our mass estimates do not include stellar kinematics in the inner regions).

### 5.1. Mass Determination

The mass contributed by the random internal motion of the galaxy (pressure-supported mass) is determined from the tracer mass estimator as

$$M_p = \frac{C}{GN} \sum_i (v_{f_i} - v_{sys})^2 R_i \quad (4)$$

where  $N$  is the number of objects in the sample and  $v_{f_i}$  is the radial velocity of the tracer object *with the rotation component removed*. For an isotropic population of tracer objects, assumed in this study, the value of  $C$  is

$$C = \frac{4(\alpha + \gamma)(4 - \alpha - \gamma)(1 - (\frac{r_{in}}{r_{out}})^{(3-\gamma)})}{\pi(3 - \gamma)(1 - (\frac{r_{in}}{r_{out}})^{(4-\alpha-\gamma)})} \quad (5)$$

where  $r_{in}$  and  $r_{out}$  are the three-dimensional radii corresponding to the two-dimensional projected radii of the innermost,  $R_{in}$ , and outermost,  $R_{out}$ , tracers in the sample. The



parameter  $\alpha$  is set to zero for an isothermal halo potential in which the system has a flat rotation curve at large distances. Finally,  $\gamma$  is the slope of the volume density distribution, which goes as  $r^{-\gamma}$ , and is found by determining the surface density slope of the sample and deprojecting the slope to three-dimensions. The tracer mass estimator uses a sample of tracer objects defined between  $r_{in}$  and  $r_{out}$ , yet it is important to emphasize that it determines the *total* enclosed mass within  $r_{out}$ .

There is also a contribution to the total mass by the rotational component, as determined in § 3.2.2 for the GCs and § 4 for the PNe. This mass component is determined from the rotational component of the Jeans equation,

$$M_r = \frac{R_{out} v_{max}^2}{G} \quad (6)$$

where  $R_{out}$  is the outermost tracer projected radius in the sample and  $v_{max}$  is the rotation amplitude. Therefore, the total mass of NGC 5128,  $M_t$ , is determined by the addition of the mass components supported by rotation,  $M_r$ , and random internal motion,  $M_p$ ,

$$M_t = M_p + M_r. \quad (7)$$

In the determination of the pressure-supported mass, one must estimate values for  $r_{in}$  and  $r_{out}$  knowing  $R_{in}$  and  $R_{out}$ . Evans et al. (2003) suggest that  $r_{in} \simeq R_{in}$  and  $r_{out} \simeq R_{out}$  for distributions taken over a wide angle. However, in this study the inner and outer radii of the chosen bins are at intermediate radial values within the distribution. Their assumption would therefore lead to an underestimate of the determined mass, since the true  $r_{out}$  can be quite a bit larger than the projected  $R_{out}$ . To correct for this contributed uncertainty, distributions of sample tracer populations were generated through Monte Carlo simulations. In the simulations, 340 GCs were randomly placed in a spherically symmetric system extending out to 50 kpc with an  $r^{-2}$  projected density, while 780 PNe were placed in the same environment extending out to 90 kpc. From the generated distributions, the value of  $C$  in Eqn. 5 was determined for both the real and projected positions of the tracer populations in each designated radial bin. This correction factor, listed in Tables 3-5 as  $M_{corr}$ , multiplies the pressure-supported mass from Eqn. 4. The same correction was applied to the full GC sample and the corresponding  $M_{corr}$  values are listed in Table 1 of Woodley (2006). These values are generally small, but in the worst case they triple  $M_p$ .

## 5.2. Surface Density Profiles

In Eqn. 5, the value of  $\gamma$  is determined for the tracer populations by deprojecting the slope of the surface density profile to three-dimensions. Figure 12 shows the surface

density profiles for the entire, metal-poor, and metal-rich GC populations, along with the PN profile. The populations were binned, following Maíz Apellániz & Úbeda (2005), into circular annuli of equal numbers of objects, providing the same statistical weight to each bin (although spatial biases may still affect the GC population in the outer regions along the major axis; see Fig. 3). In the inner 5 kpc of all tracer populations, incompleteness due to the obscuration of the dust lane is evident by the flattening of the surface density profile. The innermost objects were, therefore, excluded from the surface density profile fittings. Outside of 5 kpc, the surface densities fit well to power laws, leading to  $\gamma = 3.65 \pm 0.17$ ,  $3.49 \pm 0.34$ ,  $3.37 \pm 0.30$ , and  $3.47 \pm 0.12$  for the entire GC population, the metal-poor and metal-rich subpopulations of GCs, and the PNe in NGC 5128, respectively. These are all very similar within their uncertainties.

### 5.3. Mass Results

The similar kinematics we find between the metal-poor and metal-rich subpopulations of GCs in this study strongly justifies the combining of the two populations for the mass determination performed in Woodley (2006). The GC population provides a *total* mass estimate of  $(1.3 \pm 0.5) \times 10^{12} M_{\odot}$  from 340 clusters out to a projected radius of 50 kpc. Removing the GCs in our sample with  $v_r \leq 300 \text{ km s}^{-1}$ , which will remove all possible contamination from foreground stars, discussed in § 3.1, leads to a total mass of  $(1.0 \pm 0.4) \times 10^{12} M_{\odot}$ . This mass agrees nicely with our mass determined from our entire GC sample. The PN population provides a total mass of  $(1.0 \pm 0.2) \times 10^{12} M_{\odot}$  from 780 PNe out to 90 kpc in projected radius, agreeing with the GC value within the uncertainty.

We are also able to generate a mass profile of NGC 5128 from the total GC population and the PNe, shown in Figure 13. The tracer mass estimator determines the *total* enclosed mass for NGC 5128 within the outermost radius of a given tracer sample. It calculates this total mass using a sample of objects defined within the radial range defined by the sample’s inner and outermost radii. It is therefore possible to use a unique set of tracer objects, denoted by the radial bin range, listed in the first column of Tables 2-5, to determine a mass profile from independent mass estimates. The independent binning, leads to sample sizes in the mass determination, in some cases generating higher uncertainties in the total enclosed mass. The most certain mass is the one determined from the full sample of tracers.

In the mass determinations above, we have implicitly assumed isotropy for the velocity distributions. But the possibility exists that the PNe (for example) might have radial anisotropy which would produce their gradually falling  $\sigma_v(R)$  curve. Replacing Equation 5

in the tracer mass estimator by

$$C = \frac{16(\alpha + \gamma - 2\beta)(4 - \alpha - \gamma)(1 - (\frac{r_{in}}{r_{out}})^{(3-\gamma)})}{\pi(4 - 3\beta)(3 - \gamma)(1 - (\frac{r_{in}}{r_{out}})^{(4-\alpha-\gamma)})} \quad (8)$$

which includes the anisotropy parameter,  $\beta$ , from Evans et al. (2003), we find that the mass estimate from the PNe can be forced to agree with the mass estimate from the GCS for a nominal  $\beta = 0.8$ . For perfect isotropy,  $\beta = 0$ . This would mean roughly 2:1 radial anisotropy for the PNe in the outer halo. However, we find that any  $\beta$  in the wide range of  $-10 \leq \beta \leq 1$  would still keep the two methods in agreement within their internal uncertainties, so we are not yet in a position to tightly constrain any anisotropy. It is possible that the GCs may also have anisotropy; it may therefore be too simplistic to find a range of  $\beta$  for the PNe for which the masses of the PNe and GCs agree. However, the GCs are likelier to be nearly isotropic than the PNe; the GCs are older, "hotter" subsystems of the halo. In other studies, the isotropy of the GCS orbits has also been shown to be a good assumption from mass profiles of elliptical galaxies using X-ray observations (Côté et al. 2001, 2003; Bridges et al. 2006, among others).

Both mass estimates can be compared to previous studies. First, we note the total mass determined from the PN data with that of Peng, Ford & Freeman (2004b). While the rotationally supported mass was determined here with different values of the mean rotational velocity, they calculated the pressure supported mass using the identical tracer mass estimator technique with exactly the same PN population. The total mass estimate given by Peng, Ford & Freeman (2004b) is  $(5.3 \pm 0.5) \times 10^{11} M_{\odot}$ . Subtracting their rotationally supported mass leaves a pressure supported mass of  $\sim 3.4 \times 10^{11} M_{\odot}$ , quite different from our  $(8.46 \pm 1.72) \times 10^{11} M_{\odot}$ . Recalculating our pressure supported mass estimate with  $\gamma = 2.54$ , which was used in Peng, Ford & Freeman (2004b), we are able to reproduce their mass estimate within the uncertainty. The values of  $\gamma$  differ between the two studies simply because the  $\gamma$  used in Peng, Ford & Freeman (2004b) was the inverse of the surface density slope instead of the inverse of the volume density slope. Using the correct value of  $\gamma = 3.54$ , their pressure supported mass estimate would increase to  $8.7 \times 10^{11} M_{\odot}$ , matching the mass found in this study.

Second, we compare our total mass determined using the GC population with that from Peng, Ford & Freeman (2004c). Using 215 GCs out to 40 kpc, they found a pressuresupported mass of  $(3.4 \pm 0.8) \times 10^{11} M_{\odot}$ , again much different from our pressure supported mass of  $(1.26 \pm 0.47) \times 10^{12} M_{\odot}$  using 340 clusters out to 50 kpc. The large difference can again be attributed to their using  $\gamma = 2.72$  instead of deprojecting their surface density slope to  $\gamma = 3.72$ . Using the correct value of  $\gamma$ , we find a pressure-supported mass of  $7.5 \times 10^{11} M_{\odot}$  using the same 215 clusters they used in their study. This corrected estimate is closer to the

pressure supported mass determined in our study, but it is not necessarily expected to agree with our result, as our sample contains 130 more GCs and uses a slightly different  $\gamma$  that we have independently redetermined.

Third, the mass determined by the H I shell study of NGC 5128 by Schiminovich et al. (1994) found a mass of  $2 \times 10^{11} M_{\odot}$  *within 15 kpc* assuming a distance of 3.5 Mpc. With the distance of 3.9 Mpc used in this study, the mass determined in their study would increase to  $2.2 \times 10^{11} M_{\odot}$ , which is 30% smaller than our total mass of  $3.89 \pm 0.94 \times 10^{11} M_{\odot}$  within 15 kpc.

Lastly, we compare our determined mass to a recent study by Samurović (2006). Samurović (2006) determined a total mass of NGC 5128 using GCs, PNe, and an X-ray data technique. The galaxy mass determined from the GC and PN data was obtained using the tracer mass estimator and the spherical Jeans equation, as performed in our study. However, Samurović (2006) used the volume density slopes determined by Peng, Ford & Freeman (2004b) and Peng, Ford & Freeman (2004c), for the PN and GC data, respectively. They obtained mass estimates for NGC 5128 similar to those of Peng, Ford & Freeman (2004b) and Peng, Ford & Freeman (2004c), discussed above, using an identical PN sample and slightly increased GC sample. They also included an X-ray-modelling mass estimate for NGC 5128 from which they obtained masses of  $(7.0 \pm 0.8) \times 10^{11} M_{\odot}$  out to 50' and  $(11.6 \pm 1.0) \times 10^{11} M_{\odot}$  out to 80'. This mass estimate is similar to our PNe estimate out to the same radial extent, but the author cautions that it is an overestimate of the true mass of NGC 5128 resulting from a lack of hydrostatic equilibrium in the outer region of the galaxy.

We note here that the mass estimates obtained are higher than those from Hui et al. (1995), and Peng, Ford & Freeman (2004b) derived from the PNe using a two-component mass model, as well as Samurović (2006), using an X-ray modelling technique. This discrepancy is not fully understood and possibly lies in the assumptions that go into the mass estimators with a spatially biased sample. We intend to pursue this issue further with an upcoming larger sample of GCs with less spatial biases.

The mass of NGC 5128 that we find appears to be in the range of other giant elliptical galaxies, such as NGC 1399 ( $\sim 2 \times 10^{12} M_{\odot}$  out to 50 kpc; Richtler et al. 2004), M49 ( $\sim 2 \times 10^{12} M_{\odot}$  out to their kinematically studied radius of 35 kpc; Côté et al. 2003), and M87 ( $\sim 9 \times 10^{11} M_{\odot}$  at 20 kpc, the onset of the projected cD envelope; Côté et al. 2001). Clearly, it is legitimate to say that NGC 5128 is the largest, most massive galaxy in the neighborhood of the Local Group, and one that can be talked about in the same category as these other giants that reside in larger clusters.

The sample biases mentioned above in our currently available set of both GCs and PNe

place limitations on how much we can reasonably interpret the kinematic and dynamic data. We are currently carrying out a set of new spectroscopic programs to increase the tracer sample size and to remove the sample biases, leading to a more complete analysis of the halo velocity field.

## 6. Discussion and Conclusions

Angular momentum is an essential quantity for characterizing the sizes, shapes, and formation of galaxies and is often represented as the dimensionless spin parameter,

$$\Lambda = \frac{J|E|^{1/2}}{GM^{5/2}} \quad (9)$$

where  $J$  is the angular momentum,  $E$  is the binding energy, and  $M$  is the mass of the galaxy. The spin parameter is representative of a galaxy’s angular momentum compared to the amount of angular momentum needed for pure rotational support: the lower the  $\Lambda$ -value, the less rotation and rotational support within the galaxy. For an elliptical galaxy in gravitational equilibrium, the spin parameter simplifies to  $\Lambda \sim 0.3 < (\Omega R/\sigma_v) >$  (Fall 1979), yielding  $\Lambda = 0.10$  with  $(\Omega R/\sigma_v) = 0.33$  for the entire population of GCs in NGC 5128.

Table 6 shows the spin parameter for four giant galaxies with large GCS kinematic studies, M87, M49, NGC 1399, and NGC 5128. The table columns give the galaxy name, the rotation amplitude, the projected velocity dispersion, and the ratio of the rotation amplitude to the velocity dispersion, followed by the spin parameter. These quantities are shown for the metal-poor and metal-rich populations. What is clearly evident in Table 6 is the strong galaxy to galaxy differences between these four galaxies, already hinted at in § 1. Though the sample is still quite small, no obvious pattern emerges. There is an indication of metal-poor and metal-rich GCSs having similar spin parameters within the same galaxy. M49 is the only galaxy studied here where this may not be the case. Although the metal-poor and metal-rich cluster spin parameters are consistent within the uncertainties, the metal-rich cluster spin parameter of M49 is also consistent with zero.

In the monolithic collapse scenario, Peebles (1969) describes the angular momentum within the galaxy as attributed to the tidal torque transferred from neighbouring proto-galaxies during formation. In this scenario, Efsthathiou & Jones (1979) found that a spin parameter of  $\Lambda = 0.06$  for elliptical systems is expected from simulations of the collapse of an isolated protogalactic cloud. But NGC 5128, among many other giant elliptical galaxies, is not in isolation, and therefore not necessarily expected to reproduce such a low spin parameter. Also, the internal rotation axis changes at 5 kpc are not easily explained with

only the monolithic collapse scenario. In the monolithic collapse model, the inner regions would be expected to have more pronounced rotations. Yet all four of the galaxies with major kinematic studies presented here do not show a higher rotational signal in the inner regions. In fact, for NGC 1399, the outer region ( $R > 6'$ ) indicates rotation in the metal-poor population that is not evident in the inner regions. Also, a slightly lower rotational signal is present in the inner regions of NGC 5128 for the metal-poor population than in the outer regions.

Hierarchical clustering of cold dark matter also relies on angular momentum in a galaxy being produced by gravitational tidal torques during the growth of initial perturbations. Sugerma, Summers, & Kamionkowski (2000) have demonstrated that the tidal torque theory predicts an increase in angular momentum during the collapse, and with time, the increase in angular momentum slows. Accretion of satellites and/or merger events is therefore a possible culprit for moving the angular momentum outward, as major mergers of disks and bulges suggest that angular momentum resides largely in the outer regions of the galaxy (Barnes 1992; Hernquist 1993).

Alternatively, Vitvitska et al. (2002) examine the change in spin parameter in a scenario where the angular momentum in a galaxy is built up by mass accretion. Their results show that the spin parameter changes sharply in major merger events in the galaxy and steadily decreases with small satellite accretion events. They also show that the spin parameter for a galaxy with a major merger after a redshift of  $z = 3$  should be notably larger than a galaxy that did not undergo such a major merger. Their study obtains an average of  $\Lambda = 0.045$  from  $\Lambda$ CDM  $N$ -body simulations for galaxies with halo masses of  $(1.1 - 1.5) \times 10^{12} h^{-1} M_{\odot}$  with  $h = 0.7$ .

NGC 1399 and M49, with their weak rotation signals, are consistent with the model predictions discussed above, whereby their major formation events could have occurred at early times and with perhaps only minor accretions happening since then. However, NGC 5128 and M87 have spin parameters 2-3 times larger than predicted by the model averages. For NGC 5128, this relatively large rotation (which is nearly independent of both metallicity and radius) may, perhaps, be connected with its history within the Centaurus group environment. The rotation speed and rotation axis for its extended group of satellite galaxies are nearly identical to the NGC 5128 halo (Woodley 2006), much as if the accretion events experienced by the central giant have been taking place preferentially along the main axis of the entire group and in the same orientation. The GCS age distribution discussed by Beasley et al. (2006) and the mean age for the halo field stars (Rejkuba et al. 2005) strongly suggest that a high fraction of the stellar population in NGC 5128 formed long ago, with particularly large bursts between 8 and 12 Gyr. Even if the galaxy underwent a significant

merger perhaps a few Gyr ago (the traces of which now appear in the halo arcs and shells), the stars in it may already have been old at the time of the merger. Although a very few younger GCs have formed since then, these make up a small minority of what is present, at least for the  $R > 5$  kpc halo outside the bulge region that now contains gas and dust.

The situation for M87, with its even larger rotation signature, may require a different sort of individual history. Of the four galaxies compared here, it is at the dynamical center of the richest environment (Virgo), has the most extensive cD-type envelope, and sits within the most massive, extended, and dynamically evolved potential well. A single relatively recent major merger could in principle have caused its present high rotation, but the lack of distinctive tidal features does not necessarily favor such an interpretation and would at least suggest that such a merger should have been with another large elliptical and nondissipative galaxy. Côté et al. (2001) discuss an interpretation - at least partially resembling what we suggest for NGC 5128 - that stellar material "is gradually infalling onto M87 along the so-called principal axis of the Virgo Cluster."

In conclusion, we have presented a kinematic study of NGC 5128 that makes it now comparable to recent studies of the other giant galaxies, M87, M49, and NGC 1399. Using 340 GCs (158 metal-rich and 178 metal-poor GCs), we have calculated the rotation amplitude, rotation axis, and velocity dispersion and have searched for radial and metallicity dependences. Our findings show that both metallicity populations rotate with little dependence on projected radius, with  $\Omega R = 40 \pm 10$ ,  $31 \pm 14$ , and  $47 \pm 15$  km s<sup>-1</sup> for the total, metal-poor, and metal-rich populations, respectively. Perhaps the inner 5 kpc shows a slower rotation of the metal-poor population, but more clusters would be needed to confirm this finding. The rotation axis is  $189 \pm 12^\circ$ ,  $177 \pm 22^\circ$ , and  $202 \pm 15^\circ$  east of north for the total, metal-poor, and metal-rich populations out to a 50 kpc projected radius, assuming the velocity field is best fit by a sine curve. The rotation axis does change at 5 kpc, following the zero-velocity curve proposed by Peng, Ford & Freeman (2004b) or possibly full-on counterrotation. A study with more GCs and lower uncertainties is needed to see what is happening in the innermost 5 kpc of NGC 5128. The velocity dispersion shows a modest increase with galactocentric radius, although the outer regions (especially the metal-rich population) have less reliable statistics; this increase could be driven purely by statistical effects. We find the velocity dispersion we find  $123 \pm 5$ ,  $117 \pm 7$ , and  $129 \pm 9$  km s<sup>-1</sup> for the total, metal-poor, and metal-rich populations, respectively.

The PN data are also used to determine the kinematics of the halo of NGC 5128. These show results that are encouragingly similar to those of the GC data, except that no rotation axis change is noted with radius, and a *decrease* in velocity dispersion is found with radius, possibly indicating a difference in orbital anisotropy compared with the GCs. A

very similar effect has been noted for the Leo elliptical NGC 3379, although with a much smaller data sample (Romanowsky et al. 2003; Bergond et al. 2006; Pierce et al. 2006). We also determine the total dynamical mass using both the GCs and the PNe by separately calculating the pressure supported mass with the tracer mass estimator and the rotationally supported mass using the spherical component of the Jeans equation. The total mass is  $(1.3 \pm 0.5) \times 10^{12} M_{\odot}$  from the GC population out to a projected radius of 50 kpc, or  $(1.0 \pm 0.2) \times 10^{12} M_{\odot}$  out to 90 kpc from the PNe.

Overall, we have enough evidence to cautiously conclude that a major episode of star formation occurred about 8 – 10 Gyr ago (corresponding to a redshift  $z = 1.2 - 1.8$ ) and this may have been when the bulk of the visible galaxy was built. We still do not know just why the most metal-poor clusters show up in such relatively large numbers and appear to have ages of 10 – 12 Gyr, but this is a common issue in all big galaxies.

This kinematic study and the age study of Beasley et al. (2006) on the NGC 5128 cluster system indicate that additional spectroscopic studies to build up both the radial velocity database and age distribution can lead to rich dividends. Large GC samples are clearly needed to remove the current sample biases and to fully understand the complex kinematics and history of this giant elliptical galaxy. It seems clear as well that each galaxy needs to be individually studied to fully understand the different galaxy formation histories. We are continuing these studies particularly for NGC 5128, with the eventual aim of at least doubling the total GC sample size in this unique system.

Acknowledgements: WEH and GLHH acknowledge financial support from NSERC through operating research grants. DAF thanks the ARC for financial support.



## REFERENCES

- Arnaboldi, M., Freeman, K.C., Capaccioli, M., & Ford, H. 1994, *ESO Messenger*, 76, 40
- Arnaboldi, M., Freeman, K.C., Gerhard, O., Matthias, M., Kudritzki, R.P. Méndez, R.H., Capaccioli, M., & Ford, H. 1998, *ApJ*, 507, 759
- Baade, W., & Minkowski, R. 1954, *ApJ*, 119, 215
- Bahcall, J.N., & Tremaine, S. 1981, *ApJ*, 244, 805
- Barnes, J.E. 1992, *ApJ*, 393, 484
- Beasley, M.A., Forbes, D.A., Brodie, J.P., & Kissler-Patig, M. 2004, *MNRAS*, 347, 1150
- Beasley, M.A., Bridges, T., Peng, E., Harris, W.E., Harris, G.L.H., Forbes, D.A., & Mackie, G. 2006, in preparation
- Bekki, K., Harris, W.E., & Harris, G.L.H. 2003, *MNRAS*, 338, 587
- Bekki, K., Forbes, D.A., Beasley, M.A., & Couch, W.J. 2003, *MNRAS*, 334, 1334
- Bekki, K., & Peng, E.W. 2006, *MNRAS*, 370, 1737
- Bergond, G., Zepf, S.E., Romanowsky, A.J., Sharples, R.M., & Rhode, K.L. 2006, *A&A*, 448, 155
- Bridges, T., Gebhardt, K., Sharples, R., Faifer, F.R., Forte, J.C., Beasley, M.A., Zepf, Z.E., Forbes, D.A., Pierce, M. 2006, *MNRAS*, 373, 157
- Ciardullo, R., Jacoby, G.H., & Dejonghe, H.B. 1993, *ApJ*, 414, 454
- Côté, P., McLaughlin, D.E., Hanes, D.A., Bridges, T.J., Geisler, D., Merritt, D., Hesser, J.E., Harris, G.L.H., & Lee, M.G. 2001, *ApJ*, 559, 828
- Côté, P., McLaughlin, D., Cohen, J.G., & Blakesless, J.P. 2003, *ApJ*, 591, 850
- Dekel, A., Stoehr, F., Mamon, G.A., Cox, T.J., Novak, G.S., & Primak, J.R., 2005, *Nature*, 437, 707
- Dufour, R.J., Harvel, C.A., Martins, D.M., Schiffer, F.H., Talent, D.L., Wells, D.C., van den Bergh, S., & Talbot, R.J. 1979, *AJ*, 84, 284
- Efstathiou, G., & Jones, B.J.T. 1979, *MNRAS*, 186, 133

- Evans, N.W., Wilkinson, M.I., Perrett, K.M., & Bridges, T.J. 2003, *ApJ*, 583, 752
- Fall, S.M. 1979, *Rev. Mod. Phys.*, 51, 21
- Ferrarese, L., Mould, J.R., Stetson, P.B., Tonry, J.L., Blakeslee, J.P., & Ajhar, E.A. 2006, *ApJ*, in press (astro-ph/0605707)
- Harris, G.L.H., Geisler, D., Harris, H.C., & Hesser, J.E. 1992, *AJ*, 104, 613
- Harris, G.L.H., Harris, W.E., & Poole, G. 1999, *AJ*, 117, 855
- Harris, W. E., & Harris, G. L. H. 2002, *AJ*, 123, 3108
- Harris, W.E., Harris, G.L.H., Holland, S.T., & McLaughlin, D.E. 2002, *AJ*, 124, 1435
- Harris, G.L.H., Harris, W.E., & Geisler, D. 2004, *AJ*, 128, 723
- Harris, W.E., Harris, G.L.H., Barmby, P., McLaughlin, D.E., & Forbes, D. 2006, *AJ*, 132, 2187
- Heisler, J., Tremaine, S., & Bahcall, J.N. 1985, *ApJ*, 298, 8
- Hernquist, I. 1993, *ApJ*, 409, 548
- Hesser, J.E., Harris, H.C., van den Bergh, S., & Harris, G.L.H. 1984, *ApJ*, 276,491
- Hesser, J.E., Harris, H.C., & Harris, G.L.H. 1986, *ApJ*, 303, L51
- Hui, X., Ford, H.C., Freeman, K.C., & Dopita, M.A. 1995, *ApJ*, 449, 592
- Kraft, R.P., Vázquez, S.E., Forman, W.R., Jones, C., Murray, S.S., Hardcastle, M.J., Worrall, D.M., Churazov, E. 2003, *ApJ*, 592, 129
- Larsen, S.S., Brodie, J.P., Beasley, M.A., & Forbes, D.A. 2002, *AJ*, 124, 828
- Lee, H., & Worthey, G. 2005, *ApJS*, 160, 176
- Maíz Apellániz, J. & Úbeda, L. 2005, *ApJ*, 629, 7873
- Mamon, G.A., & Lokas, E.L. 2005, *MNRAS*, 362, 95
- Napolitano, N.R., Arnaboldi, M., Freeman, K.C., & Capaccioli, M. 2001, *A&A*, 377, 784
- Napolitano, N.R., Arnaboldi, M., & Capaccioli, M. 2002, *A&A*, 383, 791
- O’Sullivan, E., Forbes, D.A., & Ponman, T.J. 2001, *MNRAS*, 328, 461

- Peebles, P.J.E. 1969, *ApJ*, 155, 393
- Peng, E.W., Ford, H.C., Freeman, K.C., & White, R.L. 2002, *AJ*, 124, 3144
- Peng, E.W., Ford, H.C., & Freeman, K.C. 2004, *ApJS*, 150, 367
- Peng, E.W., Ford, H.C., & Freeman, K. 2004, *ApJ*, 602, 685
- Peng, E.W., Ford, H.C., & Freeman, K. 2004, *ApJ*, 602, 705
- Pierce, M., Beasley, M.A., Forbes, D.A., Bridges, T., Gebhardt, K., Faifer, F.R., Forte, J.C., Zepf, S.E., Sharples, R., Hanes, D.A., & Proctor, R. 2006, *MNRAS*, 366, 1253
- Press, W.H., Teukolsky, S.A., Vetterling, W.T., & Flannery, B.P. 1992, *Numerical Recipes in Fortran* (2nd Ed., Cambridge: Cambridge University Press)
- Puzia, T.H., Kissler-Patig, M., Thomas, D., Maraston, C., Saglia, R.P., Bender, R., Goudfrooij, P., & Hempel, M. 2005, *A&A*, 439, 997
- Reed, L.G., Harris, G.L.H., & Harris, W.E. 1994, *AJ*, 107, 555
- Rejkuba, M. 2001, *A&A*, 269, 812
- Rejkuba, M. 2004, *A&A*, 413, 903
- Rejkuba, M., Greggio, L., Harris, W.E., Harris, G.L.H., & Peng, E.W. 2005, *ApJ*, 631, 262
- Rejkuba, M., Dubath, P., Minniti, D., & Meylan, G. 2007, *A&A*, in press (astro-ph/0703385)
- Richtler, T., Dirsch, B., Gebhardt, K., Geisler, D., Hilker, M., Alonso, M. V., Forte, J. C., and Grebel, E. K., Infante, L., Larsen, S., Minniti, D., & Rejkuba, M. 2004, *AJ*, 127, 2094
- Romanowsky, A.J., Douglas, N.G., Arnaboldi, M., Kuijken, K., Merrifield, M.R., Napolitano, N.R., Capaccioli, M., & Freeman, K.C., 2003, *Science*, 301, 1696
- Saglia, R.P., Kronawitter, A., Gerhard, O., & Bender, R. 2000, *AJ*, 119, 153
- Samurović, S. 2006, *Serb. Astron. J.*, 173, 35
- Schimminovich, D., van Gorkom, J.H., van der Hulst, J.M., & Kasow, S. 1994, *ApJ*, 423, L101
- Sharples, R. 1988, *IAU Symp. 126: The Harlow-Sharpley Symposium on Globular Cluster Systems in Galaxies*, 126, 245

- Strader, J., Brodie, J.P., Cenarro, A.J., Beasley, M.A., & Forbes, D.A. 2005, *AJ*, 130, 1315
- Sugerman, B., Summers, F.J., & Kamionkowski, M. 2000, *MNRAS*, 311, 762
- Thomas, D., Maraston, C., & Korn, A. 2004, *MNRAS*, 351, 19
- Toomre, A., & Toomre, J. 1972, *ApJ*, 178, 623
- van den Bergh, S., Hesser, J.E., & Harris, G.L.H. 1981, *AJ*, 86, 24
- Vitvitska, M., Klypin, A.A., Kravtsov, A.V., Wechsler, R.H., Primack, J.R., & Bullock, J.S. 2002, *ApJ*, 581, 799
- Woodley, K.A., Harris, W.E., & Harris, G.L.H. 2005, *AJ*, 129, 2654
- Woodley, K.A. 2006, *AJ*, 132, 2424



















Table 1—Continued

Name	Old Name	RA (J2000)	Dec. (J2000)	R ( $^{\circ}$ )	<i>U</i> (mag)	<i>B</i> (mag)	<i>V</i> (mag)	<i>R</i> (mag)	<i>I</i> (mag)	$\sigma_U$ (mag)	$\sigma_B$ (mag)	$\sigma_V$ (mag)	$\sigma_R$ (mag)	$\sigma_I$ (mag)	<i>C</i> (mag)	<i>M</i> (mag)	<i>T</i> <sub>1</sub> (mag)	$\sigma_C$ (mag)	$\sigma_M$ (mag)	$\sigma_{T_1}$ (mag)	<i>U</i> − <i>B</i> (mag)	<i>B</i> − <i>V</i> (mag)	<i>V</i> − <i>R</i> (mag)	<i>V</i> − <i>I</i> (mag)	<i>M</i> − <i>T</i> <sub>1</sub> (mag)	<i>C</i> − <i>M</i> (mag)	<i>C</i> − <i>T</i> <sub>1</sub> (mag)	( $^{\circ}$ )
GC0393 R117		13 26 21.99	-42 53 45.5	12.38	20.52	20.41	19.68	19.23	18.75	0.07	0.02	0.01	0.01	0.03	20.50	19.98	19.32	0.02	0.02	0.01	0.10	0.73	0.45	0.93	0.66	0.53	1.18	4.8
GC0394 R118		13 26 22.01	-42 54 26.5	11.99	20.73	20.60	19.87	19.38	18.93	0.08	0.03	0.01	0.01	0.03	20.72	20.19	19.50	0.03	0.02	0.01	0.13	0.73	0.49	0.95	0.70	0.52	1.22	4.4
GC0395 WHH-29		13 26 22.08	-43 09 10.7	12.79	20.97	20.70	19.82	19.28	18.73	0.08	0.02	0.01	0.01	0.03	20.92	20.17	19.38	0.03	0.02	0.01	0.27	0.88	0.54	1.09	0.79	0.75	1.54	5.0
GC0396 pff_gc-093		13 26 22.65	-42 46 49.8	17.50	20.58	20.39	19.62	19.13	18.66	0.08	0.03	0.01	0.01	0.03	20.52	19.91	19.23	0.02	0.01	0.01	0.20	0.77	0.48	0.96	0.69	0.61	1.30	5.7
GC0397 WHH-30		13 26 23.60	-43 03 43.9	10.55	20.56	20.25	19.38	18.83	18.30	0.10	0.03	0.01	0.01	0.03	20.45	19.62	18.96	0.03	0.03	0.01	0.31	0.87	0.55	1.08	0.65	0.83	1.49	4.7
GC0398 pff_gc-094		13 26 23.66	-43 00 45.6	10.25	20.99	20.77	19.97	19.49	18.93	0.09	0.03	0.01	0.01	0.03	20.92	20.24	19.57	0.03	0.02	0.01	0.22	0.80	0.47	1.04	0.67	0.68	1.35	3.3
GC0399 HHH86-38/C38/R123		13 26 23.78	-42 54 01.1	12.50	19.67	19.30	18.41	17.87	17.32	0.04	0.01	0.01	0.01	0.03	19.51	18.68	17.96	0.02	0.02	0.01	0.37	0.89	0.54	1.09	0.72	0.83	1.54	4.0
GC0400 HGHH-51		13 26 23.86	-42 47 17.1	17.26	19.63	19.34	18.47	17.93	17.38	0.05	0.02	0.01	0.01	0.03	-	-	-	-	-	-	0.29	0.87	0.54	1.09	-	-	-	3.4
GC0401 AAT335187		13 26 23.95	-43 17 44.4	19.53	21.19	21.11	20.46	20.04	19.60	0.10	0.03	0.01	0.01	0.03	21.20	20.72	20.08	0.01	0.01	0.01	0.08	0.65	0.42	0.86	0.64	0.49	1.12	2.7
GC0402 pff_gc-095		13 26 25.50	-42 57 06.2	11.33	21.13	20.60	19.60	19.02	18.40	0.11	0.02	0.01	0.01	0.03	20.97	19.97	19.17	0.04	0.03	0.02	0.53	1.00	0.58	1.20	0.80	0.99	1.79	4.0
GC0403 R124		13 26 28.87	-42 52 36.4	14.08	20.32	20.17	19.42	18.96	18.43	0.05	0.02	0.01	0.01	0.03	20.28	19.69	19.02	0.02	0.02	0.01	0.15	0.75	0.46	0.99	0.68	0.58	1.26	5.4
GC0404 pff_gc-096		13 26 30.29	-42 34 41.7	28.83	21.24	20.73	19.73	19.10	18.42	0.31	0.03	0.01	0.01	0.03	21.08	20.09	19.24	0.01	0.01	0.01	0.52	1.00	0.63	1.30	0.85	0.99	1.83	5.3
GC0405 R105		13 26 33.55	-42 51 00.9	15.74	21.28	20.78	19.86	19.28	18.70	0.11	0.03	0.01	0.01	0.03	21.18	20.25	19.46	0.02	0.01	0.01	0.50	0.92	0.58	1.15	0.79	0.93	1.72	5.3
GC0406 HGHH-27/C27		13 26 37.99	-42 45 49.9	20.00	19.60	19.39	18.60	18.11	17.62	0.03	0.01	0.01	0.01	0.03	-	-	-	-	-	-	0.21	0.78	0.49	0.98	-	-	-	4.9
GC0407 WHH-31		13 26 41.43	-43 11 25.0	16.96	20.76	20.44	19.50	18.94	18.36	0.07	0.02	0.01	0.01	0.03	20.67	19.89	19.05	0.03	0.02	0.02	0.32	0.94	0.56	1.14	0.85	0.77	1.62	5.7
GC0408 HHH86-39/C39		13 26 42.03	-43 07 44.8	15.12	18.72	18.33	17.43	16.91	16.42	0.02	0.01	0.01	0.01	0.03	18.57	17.73	16.92	0.01	0.01	-	0.39	0.89	0.53	1.01	0.81	0.83	1.65	2.7
GC0409 pff_gc-097		13 26 45.40	-43 26 34.1	29.13	19.75	19.51	18.72	18.23	17.76	0.10	0.01	0.01	0.01	0.03	19.66	19.04	18.28	0.02	0.01	0.01	0.24	0.79	0.49	0.96	0.76	0.62	1.38	5.9
GC0410 HH-017		13 26 49.31	-43 04 57.8	15.41	23.21	22.54	20.80	19.87	19.06	0.67	0.11	0.02	0.01	0.03	23.32	21.63	20.13	0.05	0.03	0.02	0.67	1.75	0.93	1.73	1.50	1.68	3.19	8.3
GC0411 pff_gc-098		13 26 53.94	-43 19 17.7	24.05	19.54	19.17	18.28	17.73	17.16	0.09	0.01	0.01	0.01	0.03	-	-	-	-	-	-	0.37	0.89	0.55	1.12	-	-	-	6.3
GC0412 AAT222977		13 26 58.91	-42 38 53.4	27.82	21.18	21.02	20.34	19.84	19.38	0.28	0.03	0.01	0.01	0.03	21.16	20.64	20.02	0.02	0.01	0.01	0.17	0.68	0.50	0.96	0.62	0.52	1.14	6.6
GC0413 HH-060		13 26 59.78	-42 55 26.5	17.79	-	-	-	-	-	-	-	-	-	-	23.41	21.69	20.14	0.05	0.04	0.02	-	-	-	-	1.55	1.72	3.26	8.3
GC0414 pff_gc-099		13 26 59.82	-42 32 40.5	33.09	20.96	20.72	19.94	19.40	18.92	0.23	0.03	0.01	0.01	0.03	20.92	20.29	19.59	0.02	0.01	0.02	0.25	0.78	0.53	1.02	0.70	0.63	1.33	4.3
GC0415 pff_gc-100		13 27 03.41	-42 27 17.2	38.12	19.92	19.37	18.41	17.81	17.17	0.11	0.01	0.01	0.01	0.03	-	-	-	-	-	-	0.56	0.96	0.60	1.24	-	-	-	5.3
GC0416 pff_gc-101		13 27 21.56	-42 38 41.4	30.63	19.89	19.51	18.72	18.20	17.74	0.10	0.01	0.01	0.01	0.03	19.74	19.02	18.39	0.01	0.01	-	0.38	0.79	0.51	0.97	0.63	0.72	1.35	2.0
GC0417 pff_gc-102		13 28 18.45	-42 33 12.5	41.90	20.38	20.11	19.29	18.76	18.24	0.14	0.02	0.01	0.01	0.03	20.28	19.59	18.94	0.04	0.04	0.01	0.27	0.83	0.52	1.04	0.65	0.70	1.34	4.2

<sup>1</sup>Radial velocity measured by van den Bergh, Hesser, & Harris (1981).<sup>2</sup>Radial velocity measured by Hesser et al. (1984).<sup>3</sup>Radial velocity measured by Hesser, Harris, & Harris (1986).<sup>4</sup>Radial velocity measured by Harris et al. (1992).<sup>5</sup>Radial velocity measured by Peng, Ford, & Freeman (2004a).<sup>6</sup>Radial velocity measured by Woodley, Harris, & Harris (2005).<sup>7</sup>Radial velocity measured by Beasley et al. (2006).<sup>8</sup>Radial velocity measured by Rejkuba et al. (2007).<sup>9</sup>These objects appear starlike under HST/ACS imaging (Harris et al. 2006).<sup>10</sup>This object appears to be a M-type star based on the strong molecular bands in its spectrum (Beasley et al. 2006).<sup>11</sup>Faint globular (Harris et al. 2006).<sup>12</sup>located in the inner bulge region which is very crowded (Harris et al. 2006).<sup>13</sup>A very compact globular or star (Harris et al. 2006).<sup>14</sup>A possible globular, but slightly elliptical (Harris et al. 2006).



Table 2. Kinematic and Dynamic Solutions for the Globular Cluster System of NGC 5128<sup>1</sup>

Radial Bin (kpc)	$R_{mean}$ (kpc)	$R_{out}$ (kpc)	N	$\Omega R$ (km s <sup>-1</sup> )	$\Theta_o$ (° E of N)	$\sigma_v$ (km s <sup>-1</sup> )	$M_{corr}$	$M_p$ ( $\times 10^{10} M_\odot$ )	$M_r$ ( $\times 10^{10} M_\odot$ )	$M_t$ ( $\times 10^{10} M_\odot$ )
0-50	12.9	48.8	340	40±10	189±12	123±5	1.0	125.8±46.5 <sup>2</sup>	3.1±1.3	128.9±46.5
0-5	3.64	4.96	54	24±21	334±59	120±12	-	-	-	-
5-10	7.65	9.96	124	43±15	195±20	112±8	2.3	37.4±6.4	0.4±0.3	37.8±6.4
10-15	12.4	14.9	68	83±25	195±12	105±10	1.6	36.5±9.3	2.4±1.5	38.9±9.4
15-25	19.0	24.3	56	35±26	184±34	147±16	1.3	89.5±27.4	0.7±1.0	90.2±27.4
25-50	34.7	48.8	39	96±45	169±17	148±21	1.0	184.7±84.5	10.4±9.8	195.1±85.1

<sup>1</sup>This table is reproduced from Woodley (2006) for completeness.

<sup>2</sup>The Tracer Mass estimator determines the total mass enclosed within the outermost radius using a sample defined in the range of the inner and outer radial bins.

Table 3. Kinematic and Dynamic Solutions for the Metal-Poor Globular Cluster System of NGC 5128

Radial Bin (kpc)	$R_{mean}$ (kpc)	$R_{out}$ (kpc)	N	$\Omega R$ (km s <sup>-1</sup> )	$\Theta_o$ (° E of N)	$\sigma_v$ (km s <sup>-1</sup> )	$M_{corr}$	$M_p$ ( $\times 10^{10} M_\odot$ )	$M_r$ ( $\times 10^{10} M_\odot$ )	$M_t$ ( $\times 10^{10} M_\odot$ )
0-50	13.8	48.1	178	31±14	177±22	117±7	1.0	94.5±58.5	1.1±1.0	95.6 ±58.6
0-5	3.84	4.96	22	16±38	373±120	99±19	-	-	-	-
5-10	7.76	9.96	66	30±21	223±39	116±12	2.1	38.9±12.4	0.2±0.3	39.1±12.4
10-15	12.7	14.8	41	97±38	199±13	102±15	1.5	31.4±15.1	3.3±2.5	34.6±15.3
15-25	18.8	24.3	26	45±31	139±49	112±20	1.3	59.7±32.7	1.2±1.6	60.8±32.7
25-50	36.7	48.1	23	61±43	137±50	141±24	1.0	122.4±82.9	4.2±5.9	126.7±83.1

Table 4. Kinematic and Dynamic Solutions for the Metal-Rich Globular Cluster System of NGC 5128

Radial Bin (kpc)	$R_{mean}$ (kpc)	$R_{out}$ (kpc)	N	$\Omega R$ (km s <sup>-1</sup> )	$\Theta_o$ (° E of N)	$\sigma_v$ (km s <sup>-1</sup> )	$M_{corr}$	$M_p$ ( $\times 10^{10} M_\odot$ )	$M_r$ ( $\times 10^{10} M_\odot$ )	$M_t$ ( $\times 10^{10} M_\odot$ )
0-50	12.0	48.8	158	47±15	202±15	129±9	1.0	116.5±73.8	4.3±2.3	120.8±73.9
0-5	3.61	4.98	29	44±27	308±47	134±23	-	-	-	-
5-10	7.52	9.93	58	65±22	180±19	105±11	1.5	17.4±7.7	1.0±0.7	18.3±7.7
10-15	12.0	14.9	27	74±34	186±22	108±17	1.2	23.8±11.3	1.9±1.8	25.7±13.3
15-25	19.3	24.3	30	50±36	223±32	168±24	1.1	72.1±46.2	1.2±1.7	73.3±46.3
25-50	31.7	48.8	15	102±96	191±21	146±65	1.0	219.1±174.6	11.8±22.2	230.9±176.0

Table 5. Kinematic and Dynamic Solutions for the Planetary Nebula System of NGC 5128

Radial Bin (kpc)	$R_{mean}$ (kpc)	$R_{out}$ (kpc)	N	$\Omega R$ (km s <sup>-1</sup> )	$\Theta_o$ (° E of N)	$\sigma_v$ (km s <sup>-1</sup> )	$M_{corr}$	$M_p$ ( $\times 10^{10} M_\odot$ )	$M_r$ ( $\times 10^{10} M_\odot$ )	$M_t$ ( $\times 10^{10} M_\odot$ )
0-90	14.1	88.2	780	76±6	170±5	118±13	1.0	84.6±17.2	11.9±1.9	96.5±17.3
0-5	3.3	4.99	184	75±16	179±11	131±7	-	-	-	-
5-10	7.6	9.98	211	82±12	177±8	120±6	3.0	43.9±3.6	1.6±0.5	45.4±3.6
10-15	11.8	14.8	138	76±15	171±10	118±7	2.0	42.3±5.0	2.0±0.8	44.2±5.1
15-20	17.4	20.0	71	96±24	169±12	116±10	1.7	47.7±5.6	4.3±2.1	52.0±6.9
20-30	24.6	30.0	87	76±17	157±17	108±8	1.5	53.2±8.4	4.0±1.8	57.2±8.6
30-40	34.6	39.8	50	44±15	132±38	87±9	1.3	40.7±7.4	1.8±1.2	42.3±7.5
40-80	48.7	71.2	36	61±45	183±22	85±11	1.0	48.6±11.5	6.2±9.1	54.8±14.7

Table 6. Spin Parameters for Giant Elliptical Galaxies

Galaxy	$\Omega R_{MP}$ (km s <sup>-1</sup> )	$\sigma_{v,MP}$ (km s <sup>-1</sup> )	$(\Omega R/\sigma_v)_{MP}$	$\Lambda_{MP}$	$\Omega R_{MR}$ (km s <sup>-1</sup> )	$\sigma_{v,MR}$ (km s <sup>-1</sup> )	$(\Omega R/\sigma_v)_{MR}$	$\Lambda_{MR}$
NGC 5128	31±14	117±7	0.26±0.12	0.08±0.04	47±15	129±9	0.36±0.11	0.11±0.03
M87 <sup>8,9</sup>	186 <sup>+58</sup> <sub>-41</sub>	397 <sup>+36</sup> <sub>-14</sub>	0.47 <sup>+0.13</sup> <sub>-0.11</sub>	0.14 <sup>+0.04</sup> <sub>-0.03</sub>	155 <sup>+53</sup> <sub>-37</sub>	365 <sup>+38</sup> <sub>-18</sub>	0.43 <sup>+0.14</sup> <sub>-0.12</sub>	0.13 <sup>+0.04</sup> <sub>-0.04</sub>
M49 <sup>9</sup>	93 <sup>+69</sup> <sub>-37</sub>	342 <sup>+33</sup> <sub>-18</sub>	0.27 <sup>+0.19</sup> <sub>-0.11</sub>	0.08 <sup>+0.06</sup> <sub>-0.03</sub>	-26 <sup>+64</sup> <sub>-79</sub>	265 <sup>+34</sup> <sub>-13</sub>	0.10 <sup>+0.27</sup> <sub>-0.25</sub>	0.03 <sup>+0.08</sup> <sub>-0.08</sub>
NGC 1399 <sup>10</sup>	15±26	291±14	0.05±0.09	0.02±0.03	7±24	255±13	0.03±0.09	0.01±0.03

<sup>8</sup>Kinematic data taken from Côté et al. (2001).

<sup>9</sup>Kinematic data taken from Côté et al. (2003).

<sup>10</sup>Kinematic data taken from Richtler et al. (2004).



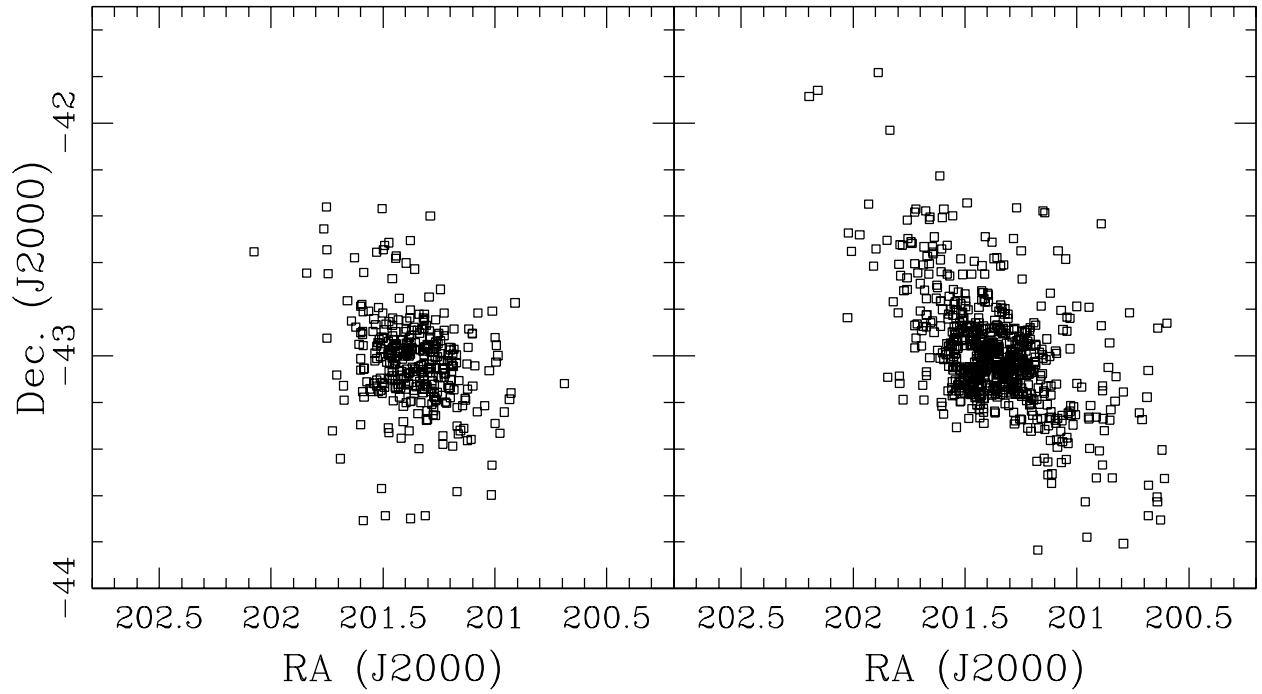


Fig. 1.— Positions of the GCS (*left*) totaling 340 objects and the PN system (*right*) totaling 780 objects in NGC 5128. The PN system has more than double the objects and extends  $\sim 40$  kpc further out from the center of NGC 5128. Both systems are spatially biased to the major axis of the galaxy with a position angle of  $35^\circ$  east of north.

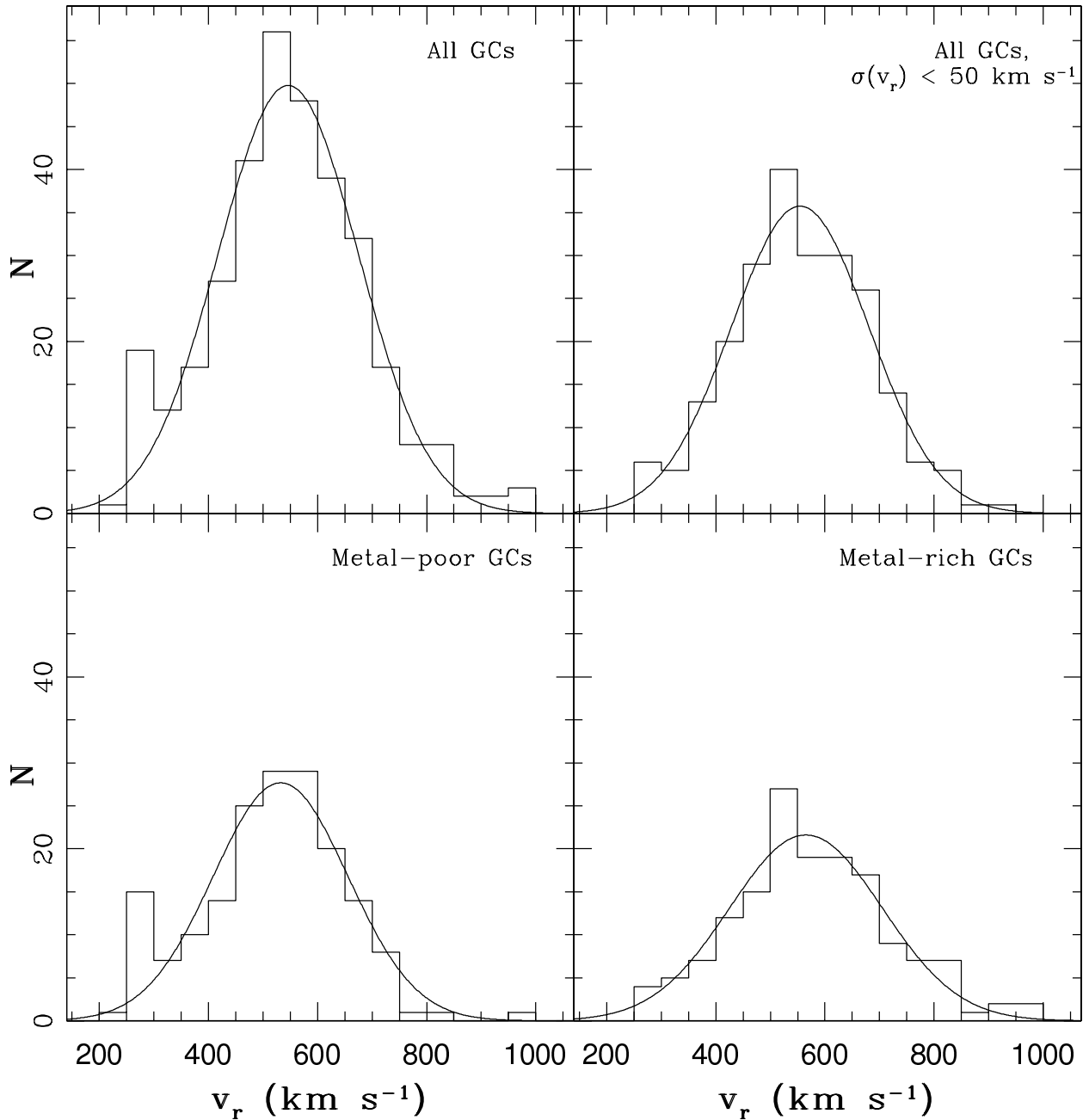


Fig. 2.— Velocity histograms fit with a Gaussian (mean velocity and standard deviation in  $\text{km s}^{-1}$ ) for the samples. *Top left*, the entire GC ( $546.4 \pm 7.3$ ,  $128.8 \pm 7.3$ ); *top right*, GCs with a radial velocity uncertainty  $< 50 \text{ km s}^{-1}$  ( $554.8 \pm 5.3$ ,  $126.2 \pm 7.3$ ); *bottom left*, all metal-poor GCs ( $532.5 \pm 12.7$ ,  $123.8 \pm 12.8$ ); *bottom right*, all metal-rich GCs ( $565.5 \pm 10.5$ ,  $140.3 \pm 10.7$ ).

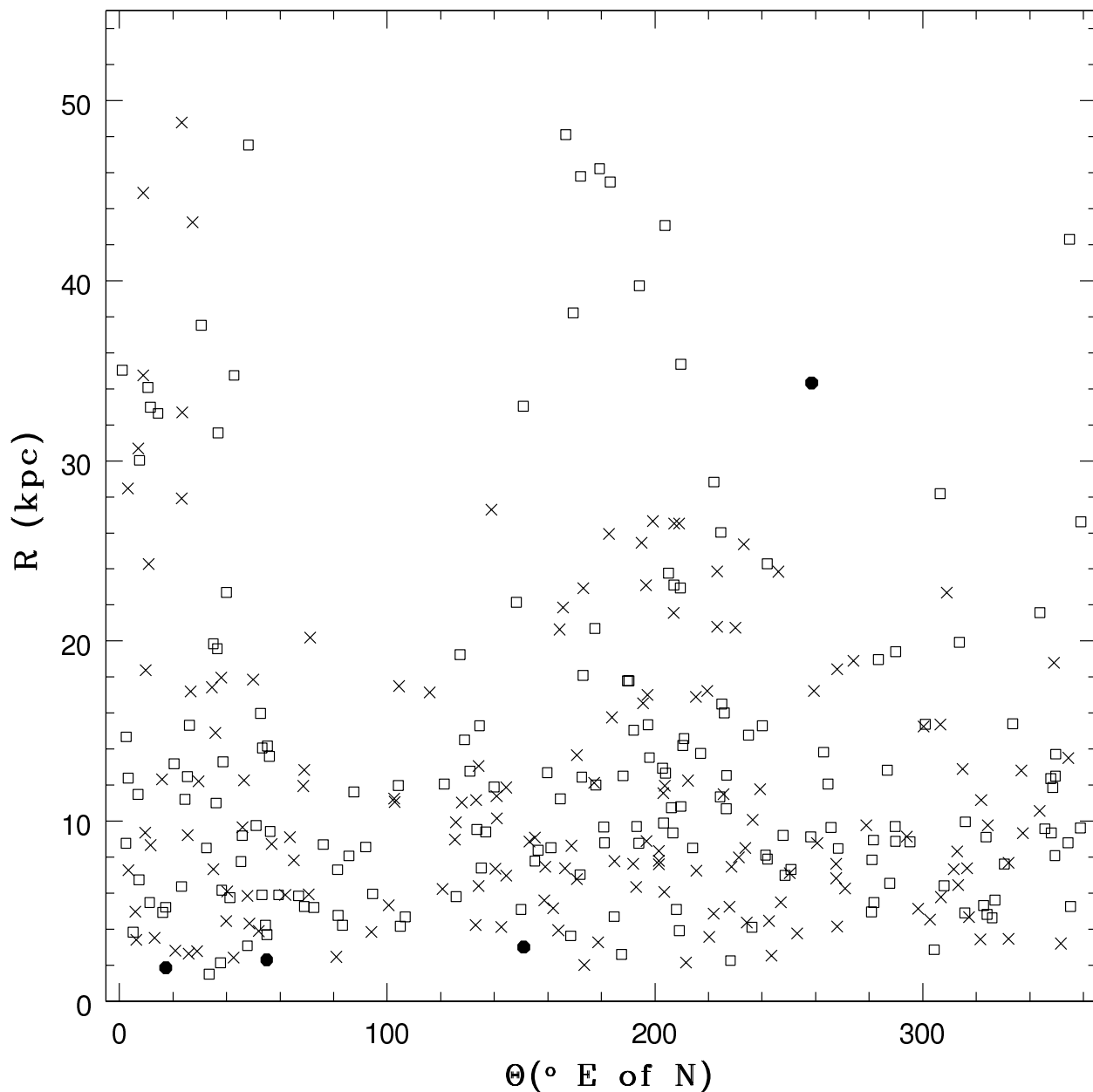


Fig. 3.— Projected radial distribution as a function of projected angular position of all known GCs in NGC 5128. The angular distribution of metal-poor (*squares*), metal-rich (*crosses*), and unknown metallicity (*circles*) subpopulations of GCs clearly shows the observational bias in GC searches along the photometric minor axis ( $\Theta = 119$  and  $299^\circ$  east of north, Dufour et al. 1979) beyond 15 kpc.

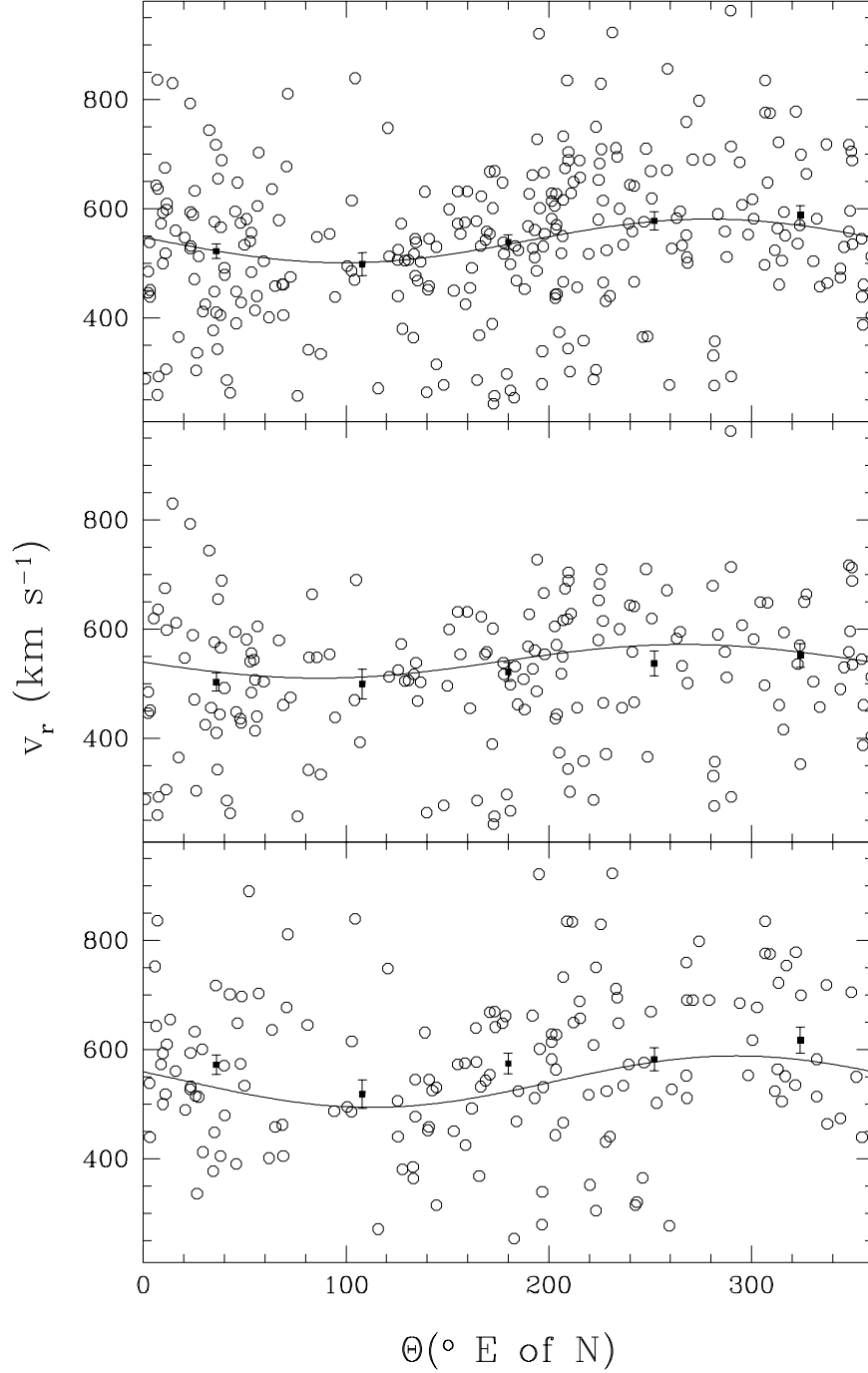


Fig. 4.— Sine curve fit for the GCs in NGC 5128 (*circles*) with a fixed systemic velocity of  $v_{sys} = 541 \text{ km s}^{-1}$ , for 0-50 kpc from the center of NGC 5128. The top panel shows all 340 GCs with rotation amplitude  $\Omega R = 40 \pm 10 \text{ km s}^{-1}$  and rotation axis  $\Theta_o = 189 \pm 12^\circ$  east of north. The middle panel shows the 178 metal-poor clusters with  $\Omega R = 31 \pm 14 \text{ km s}^{-1}$  and  $\Theta_o = 177 \pm 22^\circ$  east of north, and the bottom panel shows the 158 metal-rich clusters with  $\Omega R = 47 \pm 15 \text{ km s}^{-1}$  and  $\Theta_o = 202 \pm 15^\circ$  east of north. The squares represent the weighted velocities in  $72^\circ$  bins.

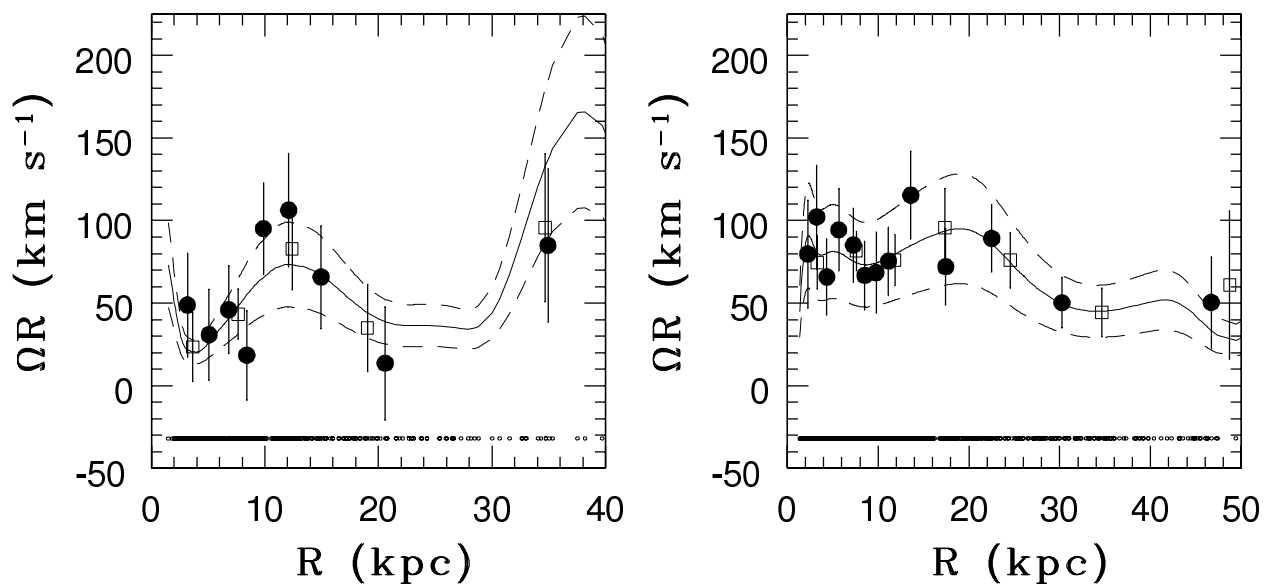


Fig. 5.— Rotation amplitude as a function of projected galactocentric radius from the center of NGC 5128, including all known GCs (*left*) and the 780 PNe (*right*). The data are binned in radial bins (*squares*) of 0-5, 5-10, 10-15, 15-25, and 25-50 kpc for the GCs or 0-5, 5-10, 10-15, 15-20, 20-30, 30-40, and 40-80 kpc for the PNe, in equal number of 38 GCs (*filled circles*) or 60 PNe, and exponentially weighted GCs or PNe with varying bin width (*solid line*) and 35% uncertainties of the weighted data (*dashed lines*). The radial distribution of data is shown at the bottom (*open circles*).

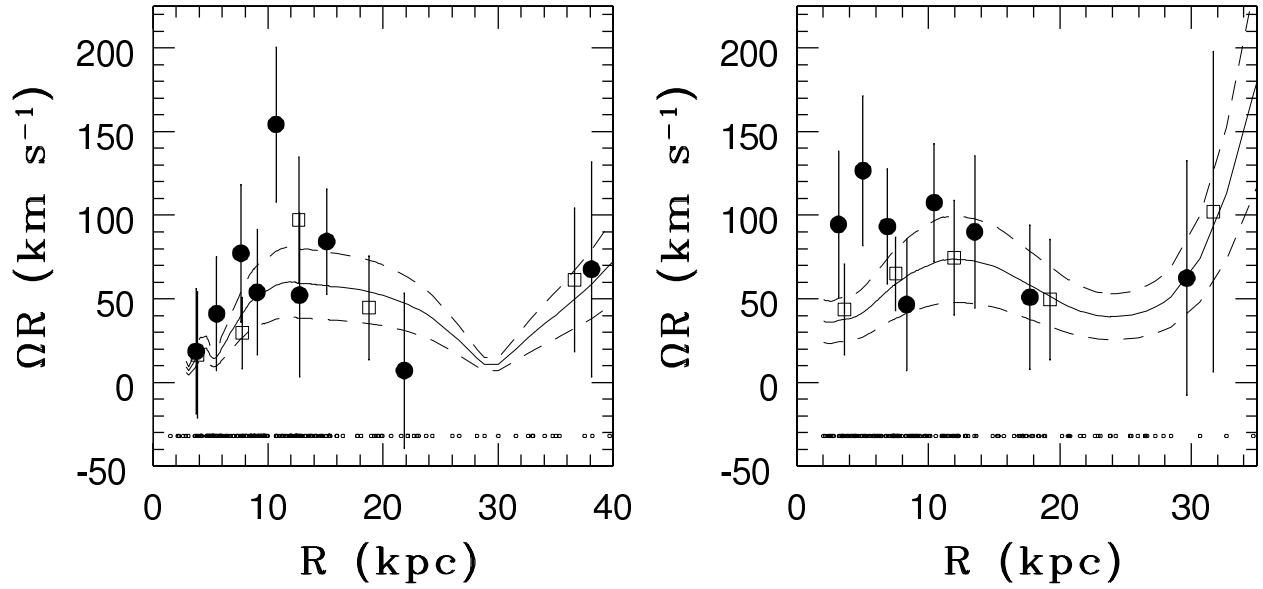


Fig. 6.— Same as Fig. 5, but for the metal-poor subpopulation of GCs (*left*) and the metal-rich subpopulation of GCs (*right*). The equal numbered bins (*filled circles*) consist of 20 metal-poor or metal-rich GCs.

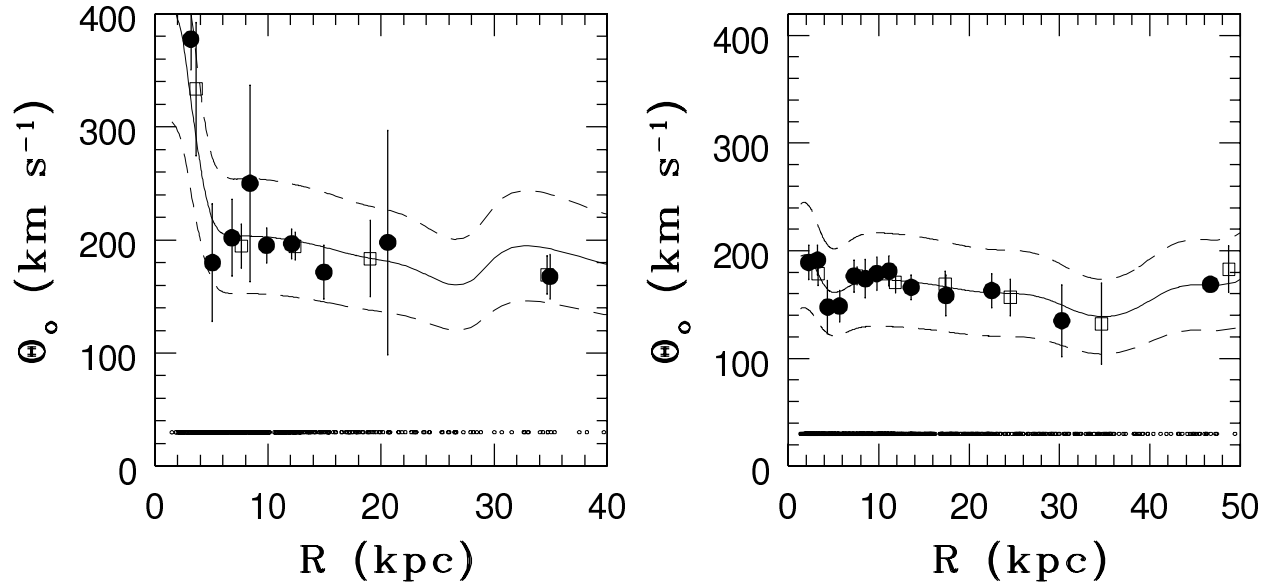


Fig. 7.— Rotation axis as a function of projected galactocentric radius from the center of NGC 5128, including all known GCs (*left*) and the 780 PNe (*right*). The symbols are the same as in Fig. 5, but the uncertainty of the weighted data (*dashed lines*) is 25%.

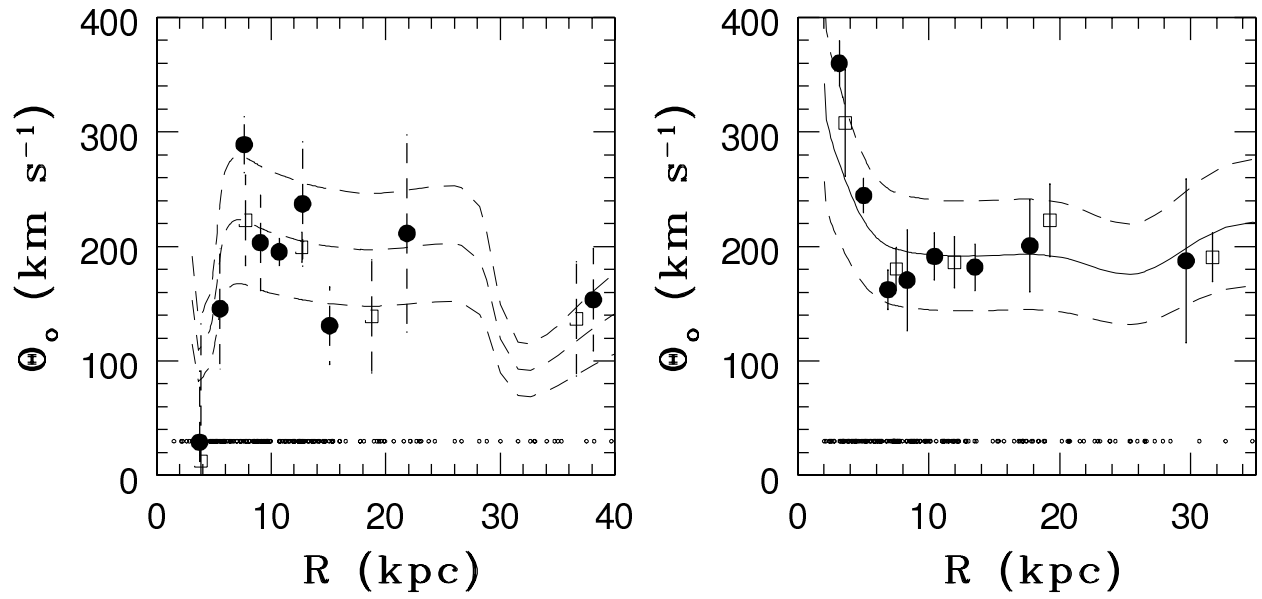


Fig. 8.— Same as Fig. 7, but for the metal-poor (*left*) and metal-rich (*right*) subpopulations of GCs.



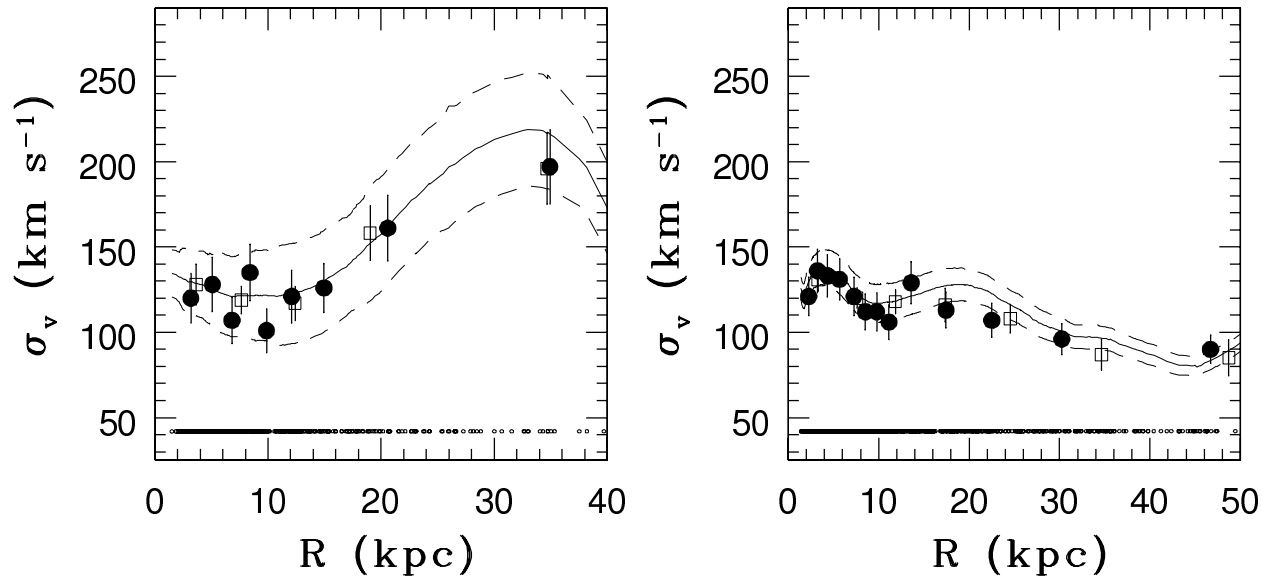


Fig. 9.— Velocity dispersion as a function of projected galactocentric radius from the center of NGC 5128 for all known GCs (*left*) and the 780 PNe (*right*). The symbols are the same as in Fig. 7, but the uncertainties of the weighted data (*dashed lines*) are determined by Eqn 2.

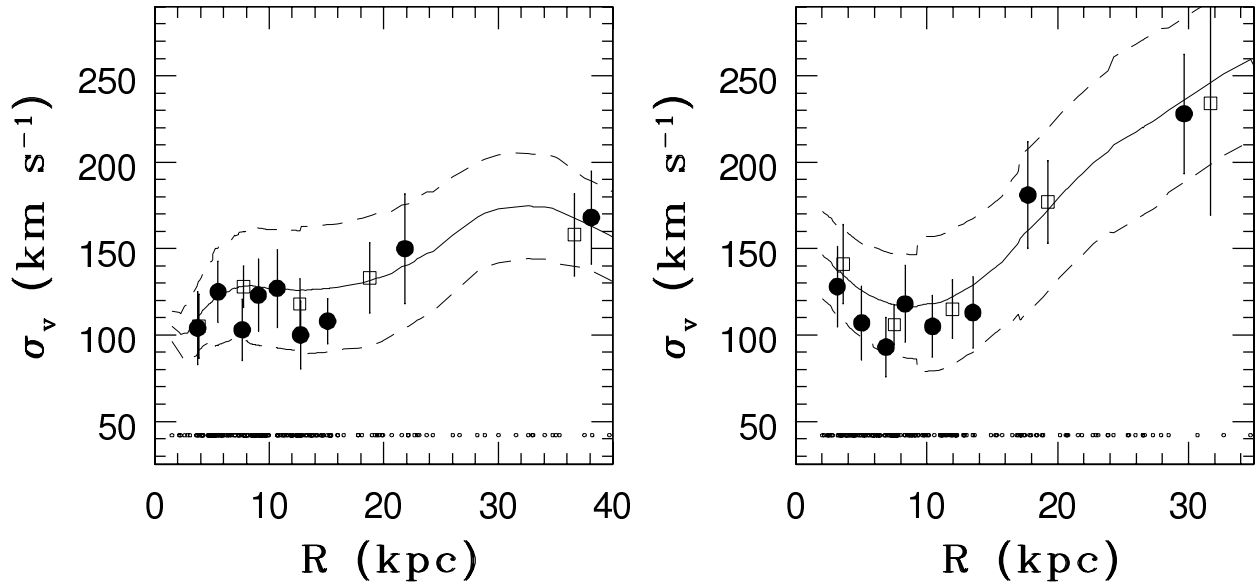


Fig. 10.— Same as Fig. 9, but for the metal-poor (*left*) and metal-rich (*right*) subpopulations of GCs.

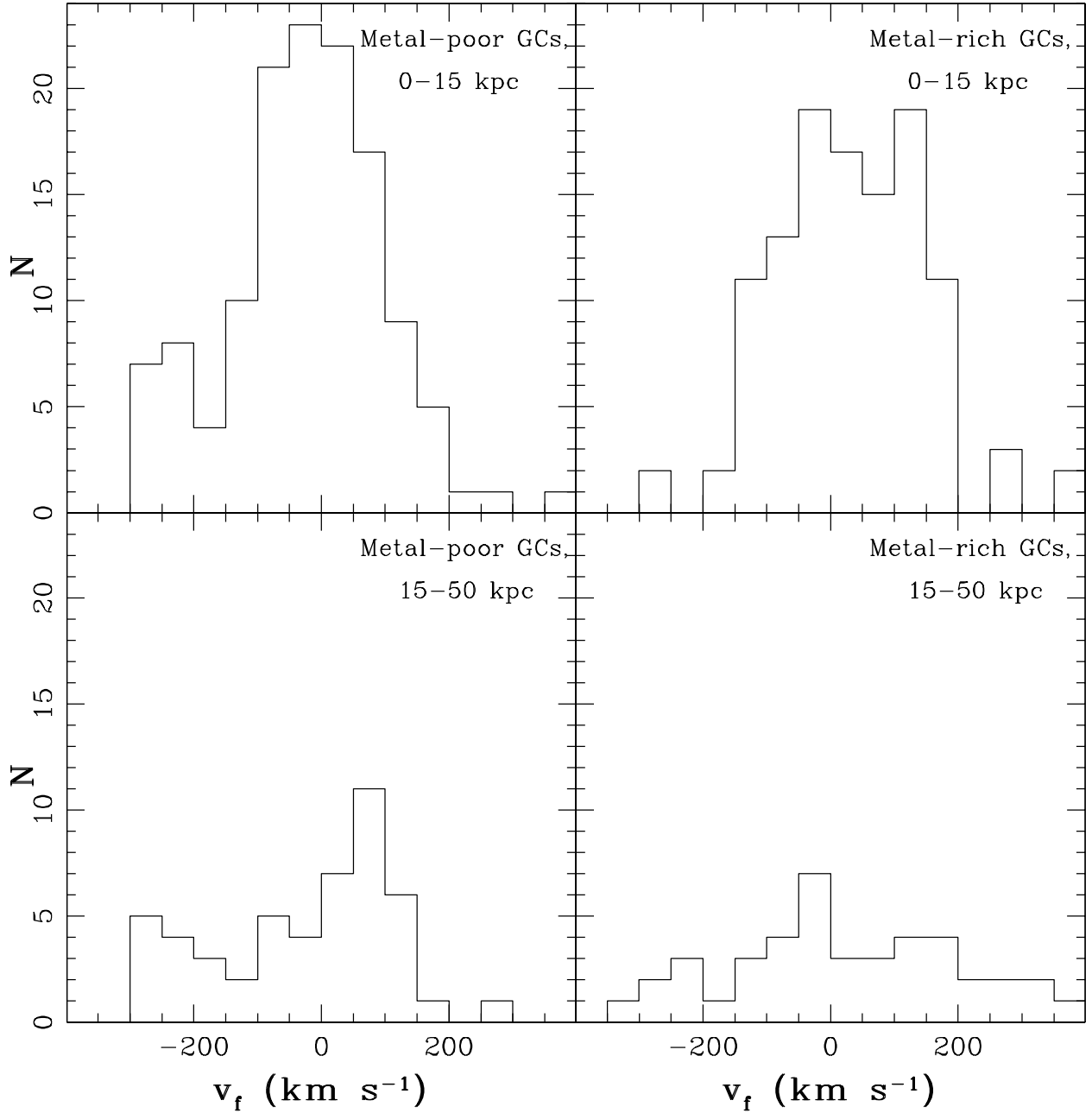


Fig. 11.— Velocity histograms for the GCs, subdivided by both metallicity and radius, binned in 50 km s<sup>-1</sup> intervals. Here  $v_f$  is the residual velocity after subtraction of the systemic velocity of 541 km s<sup>-1</sup> and the overall rotation component for either the metal-poor or metal-rich subpopulation, determined from Eqn. 1. The histograms for the metal-poor clusters (*left panels*) include 129 clusters between 0 and 15 kpc and 49 clusters between 15 and 50 kpc, while the histograms for the metal-rich clusters (*right panels*) include 114 clusters between 0 and 15 kpc and 44 clusters between 15 and 50 kpc.

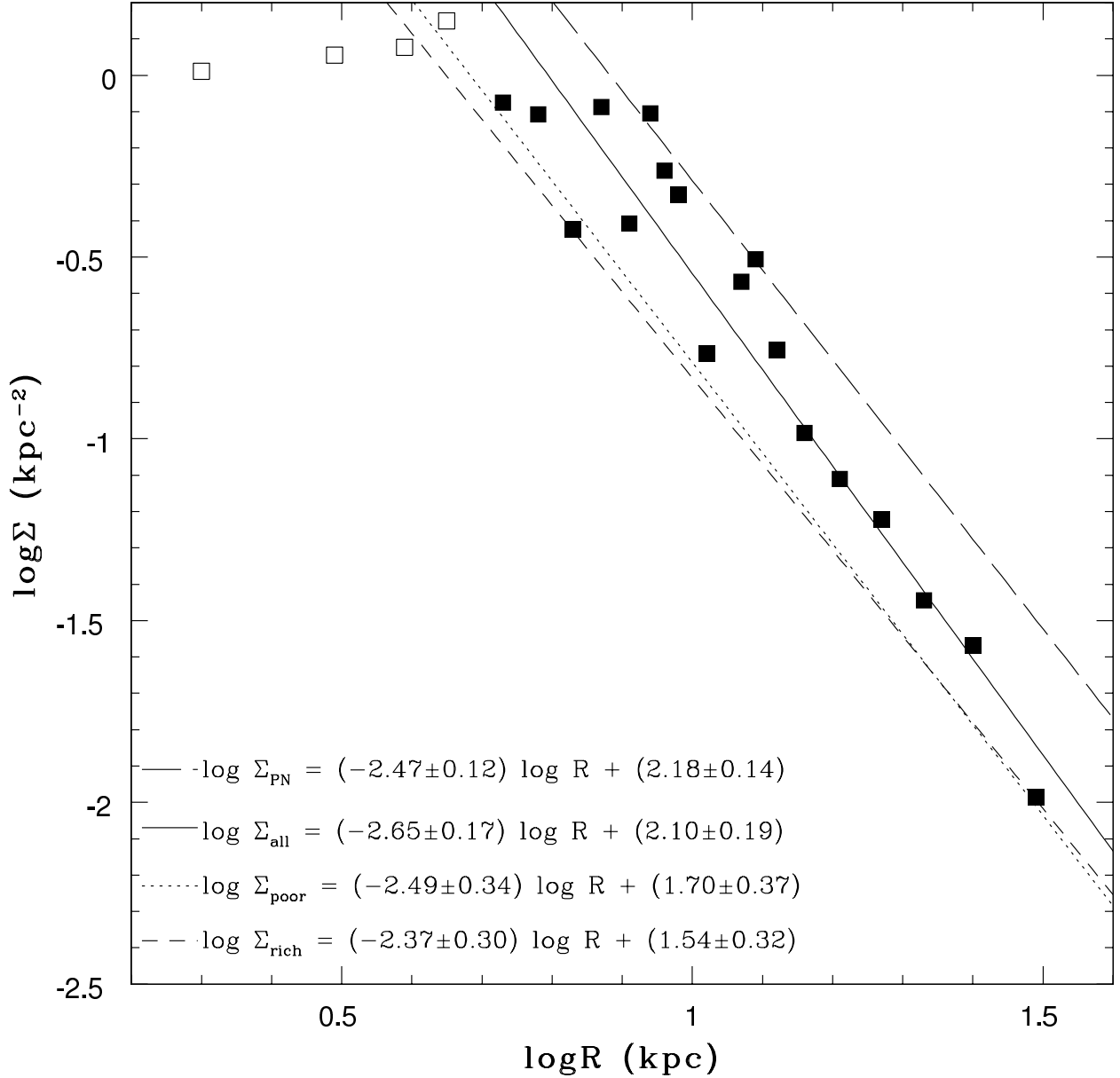


Fig. 12.— Surface density of known GCs fit with a powerlaw for the entire population (*solid line*), the metal-poor subpopulation (*dotted line*), and the metal-rich subpopulation (*short-dashed line*) in NGC 5128 with the best-fit linear coefficients shown. The radial distribution of the entire GC population is shown as filled squares, yet clusters with projected radii  $< 5$  kpc are shown as open squares and are not included in the powerlaw fits. Also overplotted is the surface density of the PN system (*long-dashed line*) fit from all PNe beyond 5 kpc with the best-fit linear coefficients also shown.

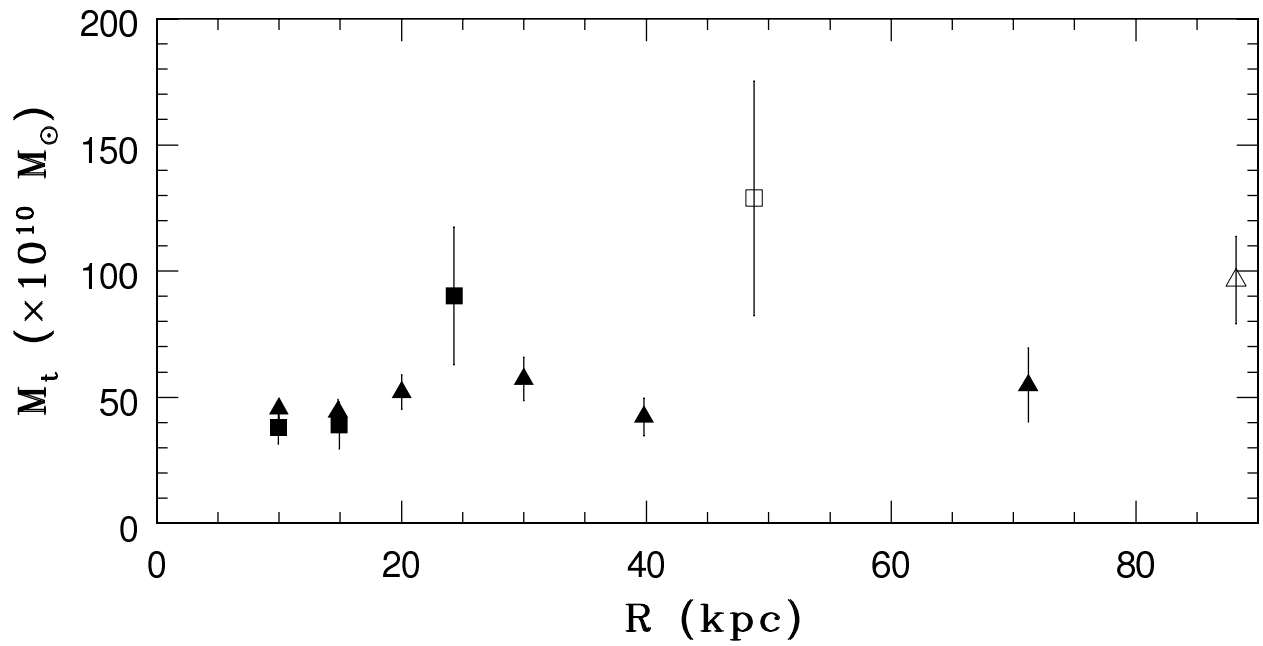


Fig. 13.— Total mass profile for the radially binned estimates of the GC system (*filled squares*) from Woodley (2006) and the PNe (*filled triangles*). The GC total mass from 0 to 50 kpc, shown as the open square, is  $1.3 \pm 0.5 \times 10^{12} M_\odot$ , and the PN total mass from 0 to 90 kpc, shown as the open triangle, is  $1.0 \pm 0.2 \times 10^{12} M_\odot$ , agreeing within the uncertainties.